A Quadrotor Sensor Platform

A dissertation presented to

the faculty of

the Russ College of Engineering and Technology of Ohio University

In partial fulfillment

of the requirements for the degree

Doctor of Philosophy

Michael J. Stepaniak

November 2008

This dissertation titled

A Quadrotor Sensor Platform

by

MICHAEL J. STEPANIAK

has been approved for

the School of Electrical Engineering and Computer Science

and the Russ College of Engineering and Technology by

Frank van Graas

Fritz J. and Dolores H. Russ Professor of Electrical Engineering

---

Maarten Uijt de Haag

Associate Professor of Electrical Engineering and Computer Science

---

Dennis Irwin

Dean, Russ College of Engineering and Technology

ABSTRACT

STEPANIAK, MICHAEL J., Ph.D., November 2008, Electrical Engineering

A Quadrotor Sensor Platform (124 pp.)

Directors of Dissertation: Frank van Graas and Maarten Uijt de Haag

A quadrotor sensor platform capable of lifting a ten pound payload is presented. Platform stabilization is accomplished using classical control methodology and is implemented on a field programmable gate array. The flight control system relies on attitude information derived using a technique that circumvents the electromagnetic susceptibility of the inertial unit while minimizing the propagation of errors.

This dissertation develops models for the high-power brushless motors. In particular, the rotational losses as a function of motor speed and the operational characteristics of the electronic speed controller are considered. Furthermore, losses within the batteries are found to dominate the power budget at planned operating speeds. Based on the models, a graphical method of predicting sortie duration is presented.

An incremental *build-up* approach is applied, leading to a successful flight test program. This platform represents a threefold increase in payload capacity for quadrotor platforms and is the largest unmanned quadrotor to successfully fly without tethers.

Approved: _____

Frank van Graas

Fritz J. and Deloros H. Russ Professor of Electrical Engineering

_____

Maarten Uijt de Haag

Associate Professor of Electrical Engineering and Computer Science

This dissertation is dedicated to my family

for their unwavering support and encouragement.

ACKNOWLEDGMENTS

TABLE OF CONTENTS

LIST OF TABLES

LIST OF FIGURES

LIST OF SYMBOLS

A	angle random walk
A_c	cross-sectional area
b_i	bit length of the initialization period
B	flux density or bias instability
B_m	sinusoidal peak flux density
$\boldsymbol{C}$	direction cosine matrix
C_D	drag coefficient
C_T	thrust coefficient
C_Q	torque coefficient
CG	center of gravity
D	drag
f	sensor data rate or motor frequency
F	force
g	gravity
$\boldsymbol{H}$	motor angular momentum
I	current
$I_{x,y,z}$	moment of inertia
$I_{xy,yz,xz}$	cross-product of inertia
$\boldsymbol{I}$	identity matrix
J_m	motor moment of inertia
k	Steinmetz core loss coefficient
k_a	anomalous core loss coefficient
k_{ch}	hysteresis correction factor
k_e	eddy current coefficient
k_h	hysteresis coefficient
K	number of intervals
K_b	back electromagnetic force constant
K_t	torque constant
K_v	voltage constant
$K_{1,2}$	rotational loss coefficients
L	x-axis moment component
l_m	motor moment arm
m	mass
M	y-axis moment component
N	z-axis moment component or motor rotations per minute
N_p	number of motor poles
N_s	number of samples total
N_τ	number of samples per integration period
p	x-axis angular rate component

P	power
q	y-axis angular rate component
Q	torque
r	z-axis angular rate component
$r_{1,2,3}$	internal resistance coefficients
$\boldsymbol{r}$	position vector
R	resistance
S_r	scaling error due to rounding
t	time
T	thrust
u	x-axis velocity component
v	y-axis velocity component
V	air velocity or voltage with subscript
$\forall$	volume
w	z-axis velocity component
θ	pitch angle
$\boldsymbol{\Theta}$	angle vector
$\boldsymbol{\Theta}_\times$	skew-symmetric form of the angle vector
ϕ	roll angle
ψ	yaw angle
ρ	air density
σ	standard deviation
σ_A^2	Allan variance
τ	integration period spanning N_τ samples
τ_i	initialization period
ω	angular rate
$\bar{\omega}_k$	mean angular rate for interval k
$\boldsymbol{\omega}$	angular rate vector
$\boldsymbol{\omega}_{arw}$	angular rate due to angle random walk
$\boldsymbol{\omega}_{bi}$	angular rate due to bias instability
$\boldsymbol{\omega}_c$	bias-corrected angular rate vector
$\boldsymbol{\Omega}_\times$	skew-symmetric form of the angular rate vector
Ω	motor speed

Subscript

a	armature
b	battery
c	core loss
e	electronic speed controller
k	discrete time interval index
m	motor

n	navigation reference frame
o	no-load
ps	power supply
r	rotational loss or command reference
rms	root mean square
t	true
T	thrust
x	body *x*-axis; aligned with a motor arm
y	body *y*-axis; aligned with an orthogonal arm
z	body *z*-axis; oriented down
0	nominal

Superscript

i	component index
b	body reference frame
t	target reference frame
α, β	Steinmetz core loss coefficients

LIST OF ACRONYMS

AEC   Avionics Engineering Center
AFIT   Air Force Institute of Technology
AFRL   Air Force Research Laboratory
DC   direct current
CG   center of gravity
DCM   direction cosine matrix
DoD   Department of Defense
ENU   East, North, up
ESC   electronic speed controller
FCS   flight control system
FAA   Federal Aviation Administration
FPGA   field programmable gate array
GPS   Global Positioning System
IEEE   Institute of Electrical and Electronics Engineers
IMU   inertial measurement unit
INS   inertial navigation system
IP   intellectual property
LCD   liquid crystal display
LED   light emitting diode
Li-Po   lithium polymer
LQ   linear quadratic
MKS   meter-kilogram-second
MEMS microelectromechanical system
NED   North, East, down
OU   Ohio University
PID   proportional-integral-derivative
PWM   pulse width modulation
RC   remote control
RPM   rotations per minute
TTL   transistor-transistor logic
UA   unmanned aircraft
UAS   unmanned aircraft system
UAV   unmanned aerial vehicle
UART   universal asynchronous receiver/transmitter
VDC   volts direct current
VHDL   VHSIC hardware description language
VHSIC very high speed integrated circuit

1 INTRODUCTION

The Global Positioning System (GPS) has become the de facto standard for precision navigation for many applications. However, the line-of-sight signals required by the GPS receiver are not always accessible in a cluttered environment, such as mountainous terrain or an urban setting. In addition, the satellite signals operate at a low power level making GPS susceptible to interference and jamming. Scenarios such as these require an alternate means of providing high level accuracy. To that end, the Avionics Engineering Center (AEC) at Ohio University (OU) has begun to investigate the ability of a scanning laser range finder, or LADAR,[1] to augment GPS.

One scenario under consideration is that of an unmanned aerial vehicle (UAV)[2] which has been navigating using GPS but then descends into a city for the next phase of its mission. Inside this *urban canyon*, access to the GPS satellite signals is blocked by towering buildings and an alternate means of navigation is required to maintain precise positioning. To maintain meter-level positioning over several minutes, a navigation-grade inertial navigation system (INS) would be required, but the cost is prohibitive for small UAVs. Instead, a line scanning LADAR, shown in Figure 1.1, updates the vehicles position and attitude using range data collected from planar surfaces [3]. The quadrotor sensor platform shown in Figure 1.2, is especially well suited for the scanning LADAR since the vehicle itself can be used to *gimbal* the sensor. In other words, small rolling and pitching motions, either commanded or incidental, will generate multiple LADAR line scans across each flat surface within the scan range. A minimum of three separate scans is required for

---

[1] LADAR is sometimes defined as an acronym for *laser radar* or *laser detection and ranging* as an analogue to radar which originally was an acronym for *radio detection and ranging*.

[2] Now termed an unmanned aircraft (UA) by the Department of Defense (DoD) [1] and the Federal Aviation Administration (FAA) [2]; part of an unmanned aircraft system (UAS) which includes the ground station and datalinks.

each planar surface to obtain a three-dimensional solution [3], but multiple scans are not possible without some means of gimbaling the LADAR.

Figure 1.1: SICK LD-OEM1000 360° scanning LADAR
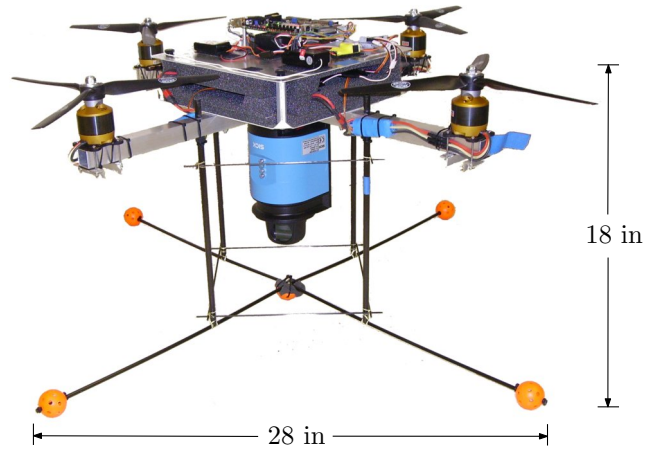
Figure 1.2: AEC quadrotor

For the urban environment, the SICK LMS-200 and the newer SICK LD-OEM1000, Figure 1.1 were identified as possessing the desired power and accuracy within a relatively small form factor. To date, the LMS-200, with a 180° line scan, has been successfully employed on the AEC autonomous lawn mower, Figure 1.3, and also on the OU search and rescue robot, Figure 1.4. Urban LADAR data was also collected in Columbus, Ohio using an LMS-200 mounted on the data collection van pictured in Figure 1.5. To expand the research to airborne platforms, a UAV with sufficient payload capacity to carry the SICK LADAR is required. A four rotor helicopter was selected for a variety of reasons.

A rotary-wing UAV has considerable advantages over a fixed-wing aircraft for this application. First, a helicopter is not required to maintain a forward velocity to sustain flight; and a heading change can be accomplished in congested areas that cannot accommodate an airplane's turning radius. Also, the ability to hover over a location allows the LADAR, or other sensors, to be continually trained on a single target for

Figure 1.3: AEC autonomous lawnmower

Figure 1.4: OU Search and Rescue Robot

Figure 1.5: AEC data collection van

surveillance, change detection, and navigation purposes. Finally, vertical takeoff and landings also minimize the launch and recover footprint and eliminate the logistical overhead of launching mechanisms such as catapults or rails used for some fixed wing UAVs.

One disadvantage of the traditional helicopter is its mechanical complexity. For example, a complex articulated rotor hub is necessary that both allows the rotor blades to flap with variation in lift and also allows for commanded changes in pitch. In addition to a single rotor for lift, traditional helicopters typically employ a vertical rotor on the tail to

compensate for the reaction torque on the fuselage caused by the main rotor [4]. Connected to the main rotor gear box, the tail rotor introduces additional complexity and, because the tail extends beyond the rotor disk, increases the area required for safe operation.

The quadrotor design overcomes these issues without compromising the advantages of the rotary wing aircraft. A pair of counter-rotating rotors balances the torque without the need for a tail rotor. The shorter rotor blades for a given disc loading [3] allows the four rotor to replace the articulated hub and thin rotor blades with simple fixed-pitch solid-hub propellers. Finally, safety can be enhanced by surrounding the relatively small rotor disks with an protective shell.

1.1 SUMMARY

This dissertation describes the design, implementation, and successful test flight of the AEC quadrotor sensor platform. This quadrotor has a greater than ten pound payload capacity and, relying solely on inertial components for stabilization, the platform is well-suited for research in GPS-denied environments. The unique contributions of this work are as follows:

1. The design, implementation, and flight test of a low-cost field programmable gate array (FPGA)-based flight control system (FCS) that provides platform stabilization without the use of GPS.

2. The demonstrated success of an attitude determination technique using an inter-ference-prone microelectromechanical system (MEMS) inertial sensor without having to physically isolate the sensor or rely on the destabilizing filters embedded in the unit.

---

[3]Disc loading is the "ratio of the all-up weight to the rotor disc area" and is an indicator of helicopter performance [4].

3. The development of models for the electronic speed controller (ESC) and the rotational losses within the motors.

4. The first flight of an unmanned quadrotor capable of lifting a ten pound payload. With a three-fold increase in payload capacity, this represents the largest unmanned quadrotor to achieve untethered free flight to date.

1.2 OVERVIEW

The remainder of this dissertation is organized as follows. Chapter 2 presents the history of the quadrotor helicopter along with a review of contemporary quadrotor UAVs. The AEC quadrotor used for this research is described at the end of the chapter. Next, Chapter 3 develops mathematical models for the following components: the brushless motors, including rotational losses, the electronic speed controller, the lithium polymer battery pack, the propeller, and the inertial sensor. Limitations of the inertial sensor, which provides attitude data necessary to stabilize the platform, are described along with a alternate method of generating attitude that minimizes the impact of these limitations. In addition, the gyroscopes contained within this sensor are characterized using an Allan Variance analysis.

The nonlinear and linearized aerodynamic models are derived in Chapter 4. Chapter 5 defines the quadrotor reference frames and then develops the navigation equations necessary to calculate attitude. Chapter 6 describes the flight control system and details its implementation on a FPGA. Preliminary actions undertaken in preparation for testing are presented in Chapter 7. These include the verification of the FCS as embedded in the FPGA, the steps included in a build up approach to flight testing, and a test hazard analysis identifying risks and mitigating procedures. The results of the attitude determination

technique are then presented in Chapter 8 along with the the flight test results. Conclusions

and recommendations are provided in Chapter 9 followed by the list of references.

2 BACKGROUND

2.1 EARLY HISTORY

Although unconventional in appearance by contemporary standards, four rotor helicopters distinguished themselves early in the development of rotary wing aircraft beginning in 1907. On August 24th of that year, the first flight of a manned helicopter took place when the Bréguet-Richet *Gyroplane No. 1* lifted off the ground in France. Depicted in Figure 2.1, the Gyroplane No. 1 featured four rotors mounted at the tips of a cross-shaped fuselage. The brief flight attained an altitude of only two feet and, because stability and control were lacking, the quadrotor motion was limited by four tethers [5].
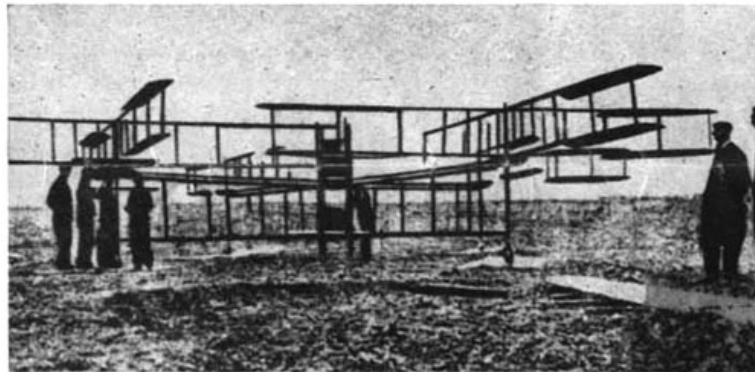
Hiller Aviation Museum (used with permission)

Figure 2.1: Bréguet-Richet Gyroplane No. 1 (1907)

In 1921 the United States Army Air Corps funded a more successful program led by Dr. George de Bothezat. De Bothezat's quadrotor, pictured in Figure 2.2, was developed in secrecy at McCook Field, predecessor to Wright-Patterson Air Force Base, Ohio, until its first flight on December 18th, 1922 [6]. In addition to the four main rotors, two additional propellers were used for directional control and two more situated above the engine provided both cooling and some additional lift. Over the next year de Bothezat

conducted over 100 test flights. One notable example highlighted the quadrotor's stability by flying with three men hanging below three of the four engines to provide an asymmetric weight distribution [5]. De Bothezat received additional funding to demonstrate improved performance, but when it failed to yield anticipated results and the Army Air Corps cancelled the program in 1923 [6].

National Museum of the Air Force

Figure 2.2: De Bothezat's quadrotor flying at McCook Field (1922)

Later, Etienne Oemichen established the viability of the quadrotor configuration when he set the Fédération Aeronautique Internationale's helicopter distance record on April 14, 1924. Oemichen went on to fly over one thousand test flights with his quadrotor, pictured in Figure 2.3, which also used additional propellers for control [5]. By 1956, D. H. Kaplan had further refined the quadrotor and demonstrated the ability to control aircraft attitude using differential thrust between pairs of rotors. This concept was tested on the H-frame Convertawings Model A [5]. Although the Model A never entered into production, the use of differential thrust for control has carried forward to the contemporary four rotor model aircraft and research testbeds.
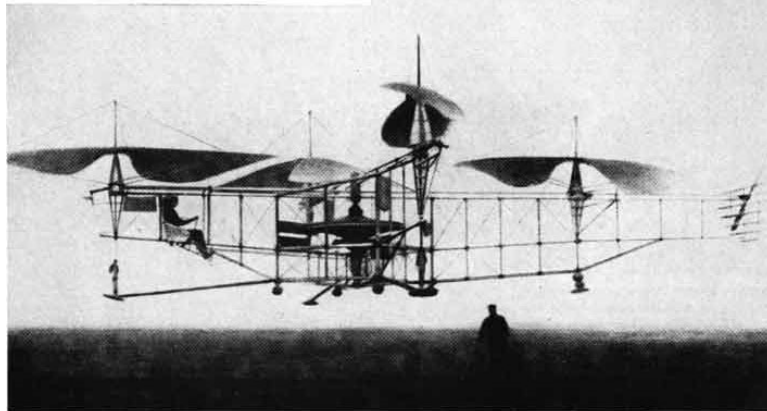
Hiller Aviation Museum (used with permission)

Figure 2.3: Oemichen's record setting quadrotor (1924)

An early quadrotor UAV was built by the Paisecki Aircraft Corporation to meet naval requirements for a weapons delivery platform launched from naval destroyers. The PA-4 *Sea Bat* achieved hover and maintained a level attitude during a tethered flight in 1958 using differential tilt for control [7]. Then, except for experimental tilt-rotors, which rotate the engine nacelles to transition between rotary wing and fixed wing modes of operation, the quadrotor design fell out of favor for the next half century.

2.2 RECENT DEVELOPMENTS

In the last decade there has been a resurgence of interest in the quadrotor configuration for unmanned aerial vehicles (UAV). Initial research into quadrotor UAVs were spurred by the introduction of radio-controlled models intended for hobbyists but with interesting characteristics particularly in the area of flight control. For example, the Draganflyer series of quadrotor aircraft has been the subject of research cooperative control testbeds at Stanford [8] and the Massachusetts Institute of Technology [9]. Also, a team at the Georgia Institute of Technology submitted a quadrotor design as their entry in the 2000 American Helicopter Society's student design competition [10]. The effort adapted a Roswell Flyer

(the precursor to the Draganflyer) to model the Martian rover and validate the aircraft dynamics and flight control [11]. Derived from a lightweight model aircraft, the payload capacity of these platforms is limited. The Draganflyer III, for example, supports about four ounces [8].

More recently quadrotor UAVs equipped with optical cameras for reconnaissance have reached the market. For instance, the European Aerospace Defence and Space Company (EADS) demonstrated a live video feed from their 500 gram Quattrocopter at the 2003 Paris Air Show [12]. Other examples are the commercially available Microdrone MD4-200 [13] and the Draganflyer V [14], both of which are capable of transmitting live video images back to the operator. Although more similar in mission to the AEC quadrotor, even the biggest, the planned Microdrone MD4-1000 is limited to a projected payload of 2.6 pounds [15].

A few research organizations have pursued original designs rather than modify the remote control (RC) quadrotors. Researchers at the Australian National University designed and built an *X4-Flyer* as an experimental robotics testbed with a 1 kg payload. In 2002, tethered flight demonstrated that a classical "double lead" compensator was sufficient for remotely piloting the vehicle. They did note a slow, controllable but unstable mode that was related to insufficient modeling of the rotor blade flapping [16]. An improved X4-Flyer Mark II was then built which featured custom-built rotor blades and a "sprung teetering" hub to address instabilities related to the blade flapping [17]. However, "chaotic semi-stable behavior" was encountered when flown tethered which precluded advancing to free flight [18].

Pennsylvania State University investigated the feasibility of building a quadrotor using commercial-off-the-shelf components. Their design was controlled using an 8-bit microcontroller and a proportional-integral (PI) control law for a remotely piloted scenario.

The airframe, however, proved too flexible and the ground tests never progressed beyond a two degree of freedom training stand [19]. Stanford University was more successful with their diminutive Mesicopter, a microelectromechanical systems (MEMS) quadrotor that achieved tethered flight. The Mesicopter team also noted an unstable mode that was overcome with two independent methods. The first was to apply rate feedback and the second was to cant the rotors slightly inward [20].

Two smaller quadrotors have been designed and flown for modeling and controls research, the French-built X4-Flyer [21], no relation to the larger Australian vehicle of the same name, and the Swiss Federal Institute of Technology's OS4, which has a total weight of just over one pound [22]. At the Korean Institute of Industrial Technology, a calamity observation quadrotor has been built with over three pound of usable payload. Equipped with 13 infrared and ultrasonic range sensors, an inertial navigation system (INS), and a video camera, the large quadrotor weighs 24 pounds without batteries [23]. Finally, the cooperative controls quadrotor platform at Stanford's has been enlarged to now supports a three pound payload. Termed the STARMAC II, the quadrotor has been tested with various sensors to include a stereo vision camera and a low-power LADAR [24].

With the payload capacity of existing quadrotors limited to the range of four ounces to three pounds, none are capable of carrying even the lighter of the two SICK LADARs, the six pound LD-OEM1000. With a design payload of ten pounds, the AEC quadrotor, described in the next section, represents a three-fold increase in payload capacity.

2.3 PRINCIPLE OF OPERATION

The AEC quadrotor is controlled using the method of differential thrust and torque that was developed for the Convertawings Model A. The motors are arranged in pairs of counter-rotating motors so that, nominally, the reaction torque generated from the first

pair of motors is exactly opposed by the reaction torque from the second pair of motors, which are spinning in the opposite direction. With balanced torques, there is no rotating moment and the body does not yaw about the vertical axis. This situation is pictured in Figure 2.4 where, if the thrust to each motor is equal to one-fourth of the vehicle's weight, the quadrotor will maintain a stationary hover. The arrows drawn around the motors indicate the speed and direction of rotation. A wider arrow would indicate a faster motor, corresponding to increased thrust and torque. Altitude is controlled by increasing or decreasing the thrust from each motor by the same amount so that total thrust changes but total torque on the body remains zero. In Figures 2.4–2.7, the *nose* of the vehicle is pointing to the right.

Figure 2.4: Balanced thrust resulting in a hovering platform

Figure 2.5 illustrates the application of differential thrust. The darker arrows indicate the two motors that have changed speed. With differential thrust applied within a pair of opposing rotors, there is no change in total thrust. In addition, the torque about the vertical axis remains zero since the decrease in torque on the slower motor is balanced by the increase in torque on the other motor since both are spinning in the same direction.

The split in thrust between the two motors, however, will induce a moment. In Figure 2.5, the moment is about the positive *x*-axis, as indicated, and the vehicle will roll to the right. Reversing the sign of the differential thrust would cause the vehicle to roll to the left. Similarly, differential thrust applied to the other pair of motors would result in either a pitch up, as shown in Figure 2.6, or a pitch down moment depending on the sign.
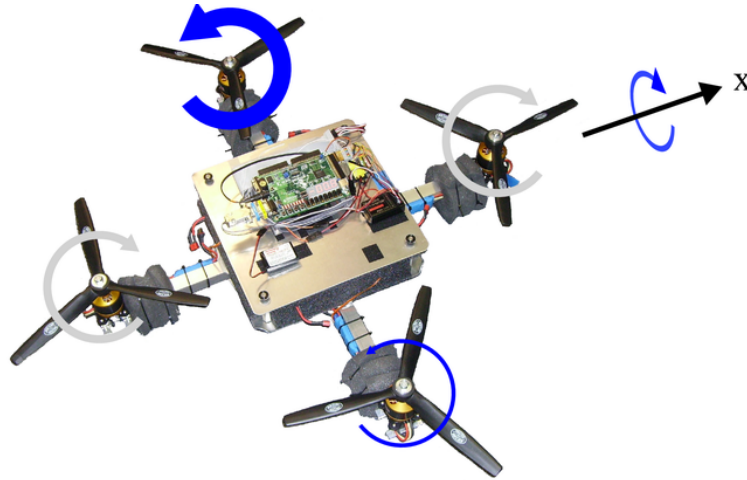
Figure 2.5: Differential thrust resulting in a rolling moment
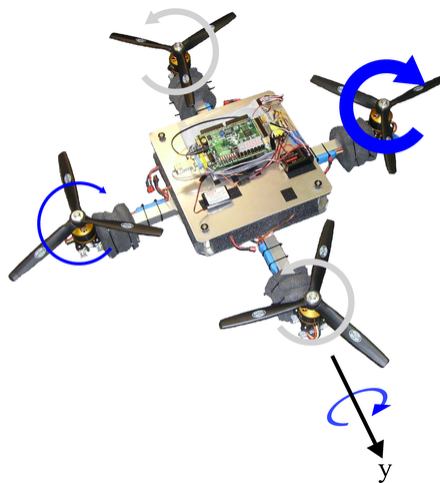
Figure 2.6: Differential thrust resulting in a pitching moment

When a thrust differential causes the quadrotor to pitch or roll, the total thrust vector is inclined away from the vertical. As a result, part of the lift vector is resolved into the horizontal plane causing a translational acceleration. For example, in Figure 2.5 the quadrotor is rolling to the right. This tilts the lift vector to the right and causes an acceleration in that direction, i.e. the quadrotor would begin to move towards the bottom of the page. With the lift vector tilted away from the vertical, there is also a corresponding loss in altitude as the amount of thrust directed vertically, in opposition to gravity, is reduced. In practice, however, with small angles of rotation, the change is minimal and hardly noticed by the pilot. Extreme changes in the pitch or roll angles, however, would cause the platform to quickly drop in altitude.

A change in azimuth is commanded by applying a differential torque to the two pairs of rotors, as shown in Figure 2.7. Because the total thrust remains constant, there is no change in altitude, but the imbalance in torque causes the body to yaw about the vertical axis, or z-axis.
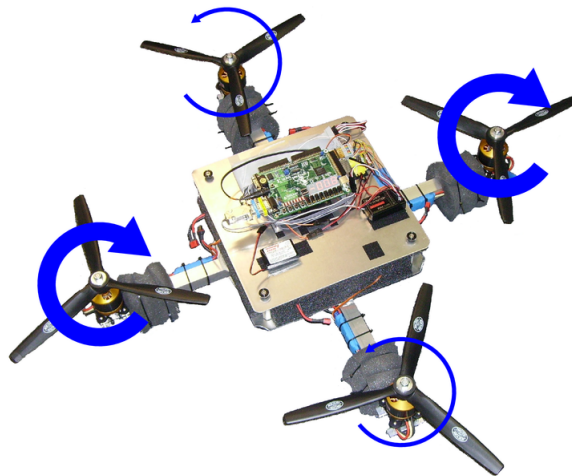
Figure 2.7: Differential torque resulting in a yawing motion

The four operations, balanced thrust, differential thrust about the roll axis, differential thrust about the pitch axis, and differential torque, depicted in Figures 2.4–2.7 represent the only means of controlling the quadrotor.

2.4 QUADROTOR CONFIGURATION

Designed and built at the AEC, the quadrotor is designed around a custom built aluminum frame with carbon fiber landing gear. The propulsion and wireless radio link consist of commercially available RC components. The navigation and control system is based on a MEMS inertial sensor and an FPGA board that hosts the closed loop stabilization routines. The quadrotor airframe, propulsion system, and radio link will be further discussed with detailed models for the various components developed in the next chapter.

2.4.1 Airframe

The basic airframe is a cross-shaped structure built from one-inch square aluminum tubing. Bolted on top of this cross-frame is a 12 inch square enclosure that contains four lithium polymer battery packs supported by foam. The bottom of the battery enclosure is an aluminum plate that adds structural integrity to the cross-frame. A second plate at the top of the battery enclosure protects the batteries and also provides a mounting surface for various electronic components.

A carbon fiber structure attached to the bottom of the cross-frame serves as both landing gear and as a protective enclosure for the LADAR. The LADAR is mounted inverted to the bottom of the cross-frame where it has a 360° field of view obstructed only by four vertical carbon-fiber rods that extend down to the landing gear. Without the payload, the AEC quadrotor weighs 16.5 lbs and there is a 42 inch span between the tips of opposing

rotor disks. Other than the aluminum airframe, the quadrotor was built using off-the-shelf components.

2.4.2 Propulsion

Propulsion is generated by four Model Motors AXi 4120/18 direct current (DC) brushless motors located at the ends of each cross-frame arm. Each motor is capable of sustaining a continuous 40 amps with the ability to surge to 55 amps for up to 60 seconds. The 14 inch propellers are mounted directly to the motor shaft, eliminating the complexity and weight associated with gear boxes. Master Airscrew MA1470T propellers are mounted on two opposing motors and MA1470TP counter-rotating propellers are mounted on the other two motors. The availability of matched counter-rotating propellers was critical in the selection of the propeller, as the control of a quadrotor relies on balancing the moments generated by opposing pairs of motors (see Section 2.3).

Power for each motor was provided by a Thunder Power TP8000-5S4PL lithium polymer (Li-Po) battery pack rated for 80 amps continuous current and featuring an 8 amp-hour capacity. Each battery pack weights 1.75 lbs and delivers a nominal 18.5 V. For each motor and battery pair, a Jeti Advance 70 Opto Plus ESC was required to convert the DC battery power to a three-phase waveform capable of driving the brushless motors at the desired speed. The ESCs are mounted on the side of each cross-frame arm just outside of the battery enclosure.

2.4.3 Control

Wireless control was accomplished using the Futaba T6EXAP digital radio pictured in Figure 2.9 and paired with a Futaba FP-R127DF seven channel receiver mounted on top of the vehicle. This radio link is typical of that used by hobbyists to fly RC aircraft. Distinct in

the AEC quadrotor, though, is the use of a Xilinx/Digilent Spartan-3 FPGA board to blend the radio commands with feedback from a Microstrain 3DM-GX1 inertial measurement unit (IMU) in order to generate the motor commands sent to the ESCs. All of the avionics components are mounted to the top of the battery enclosure and are powered by a 7.4 V Thunder Power Li-Po battery pack with a 900 mAh capacity. While the IMU is powered directly from the battery, a Draganflyer 5.1 V regulator is used to power the radio receiver and FPGA board. Figure 2.8 shows an electrical schematic showing the power and signal interconnections between the various components.
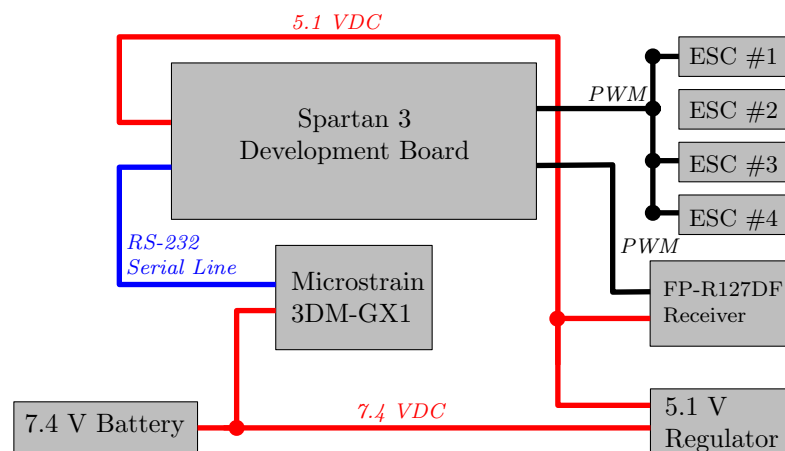
Figure 2.8: Avionics Interconnects.

The digital radio provides six channels of operation: left and right sticks, each with two-degrees of motion, a toggle switch on the top left of the radio, and a rotary dial on the top right. The two sticks are employed in a manner analogous to the collective and stick in a manned helicopter. Raising the left stick increases power collectively to all four motors[1] while the right stick controls roll and pitch[2]. In lieu of rudder pedals, the horizontal motion of the left stick is used to control yaw through the application of differential torque. Finally,

---

[1]The AEC quadrotor uses fixed pitch rotor blades so increasing the *collective* changes motor RPM and not blade pitch.

[2]Through differential thrust, as described in Section 2.3,and not by a cyclic change in blade pitch

the left-hand toggle switch is implemented as a *master arm* switch and the right-hand dial is currently unused.

Figure 2.9: Digital remote-controlled radio.

The radio also features a digital trim switch for each of the four channels controlled by the two sticks. The trim switches are just visible in Figure 2.9; they are in the chromed area near the center of the radio with one below and one to the inside of each switch.

2.4.4   Pulse Width Modulated Signals

The radio receiver and ESCs operate using pulse width modulation (PWM) signals as is typical for components built for RC models [25]. The signal has a 20 ms period and each pulse is composed of two parts: a logic high fixed at 1 ms in duration followed by a variable logic high with duration ranging from 0–1 ms. The RC components were intended for transistor-transistor logic (TTL)-level signals but work satisfactorily with the 3.3 V signals provided by the FPGA development board. Since the full range of motion is described by the variable part of the signal, which corresponds to 50,000 FPGA clock

cycles, the theoretical resolution of the PWM signal by the FPGA is 1/50,000. The PWM signal structure is illustrated in Figure 2.10.
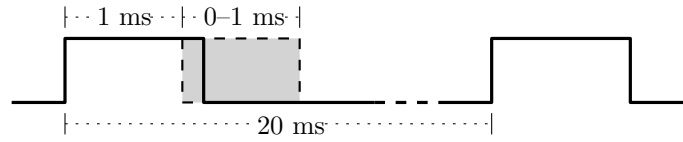
Figure 2.10: Pulse width modulated signal structure.

3 COMPONENT MODELING

3.1 BRUSHLESS MOTOR

A ten pound payload is enabled by efficient, high power brushless direct current (DC) motors coupled with high energy density lithium polymer batteries. Brushless motors replace the field windings with permanent magnets located on the rotor and move the armature windings to the stator. In this manner, the need for brushed mechanical commutation is eliminated, reducing noise and electromagnetic interference due to arcing. Without the friction of the brushes against the rotor, there is also some gain in efficiency. In addition, maintenance is greatly reduced as there are no brushes to replace. On the other hand, a disadvantage of the brushless motor is the need to perform the commutation electronically in a separate unit, as will be discussed in the following section.

A relatively new type of brushless DC motor uses an outrunner configuration where the base and armature windings are fixed to the airframe and the outer case spins as part of the rotor [26]. In this manner, a greater number of permanent magnets can be attached to the rotor resulting in a *magnetic gearing* effect [27] that provides a greater amount of torque at low speeds without the need for mechanical gearing. High power outrunner motors were therefore selected to directly drive the 14 inch diameter propellers, eliminating the complexity and weight associated with gear boxes.

3.1.1 Motor Constants

In an ideal direct current motor the desired motor speed is set by controlling the armature voltage and allowing the motor to draw sufficient current to drive the propeller. Real efficiency, however, is decreased by electrical and mechanical losses, one of which is the copper loss. Accounting for the power dissipated as heat in the armature windings,

copper loss is modeled as an armature resistance, R_a, as shown in Figure 3.1. Note that the inductance of the armature has been omitted from this model as the electrical time constant will be insignificant compared to the mechanical time constant [28]. A second loss that impacts efficiency, the iron or core loss, will be considered later.
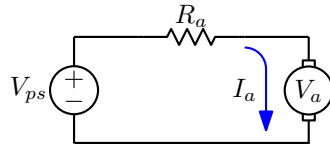
Figure 3.1: Basic Motor Model

Without the ability to vary gearing to achieve the desired torque for a given motor speed, however, the motor selection is more critical. The governing relationships between motor speed and torque, N and Q, respectively, and armature voltage and current, V_a and I_a, respectively, are

$$Q = K_t I_a \tag{3.1}$$

$$N = K_v V_a \tag{3.2}$$

where K_t and K_v are the torque and voltage constants, respectively. For motors used in remote control applications, these constants are typically published with units of oz·in/A and RPM/V, respectively. From Equations (3.1) and (3.2), the product of K_v and K_t is the ratio of mechanical power to electrical power and, with consistent units, the ratio would be unity. In the units of oz·in/A and RPM/V the relationship becomes:

$$K_v K_t = 1352 \tag{3.3}$$

The implication of the inverse relationship between K_v and K_t is that a motor that spins fast (high K_v) will need to draw a high current to produce a given amount of torque (low K_t), and vice versa. The goal then is to select a motor with a pair of constants that will

generate the desired thrust, a function of motor speed, at a current draw, proportional to torque, that is within the specified limits of the motor. Because the relationship between thrust and torque is governed by the design of the propeller used, a propeller model must be matched to the motor model in order to quantify the performance of a given motor. Without published aerodynamic coefficients, data collected from a thrust test stand can be used to generate the propeller model.

3.1.2 Determining Motor Parameters

Specific motor parameters can be determined using data collected from an unloaded motor. Because the armature resistance is less than $100\ \Omega$ it cannot be measured directly with a digital multimeter. Instead, Ohm's law is used to calculate the resistance as the ratio of the applied voltage from the power supply to the current through the motor armature:

$$R_a = \frac{V_{ps}}{I_a} \tag{3.4}$$

Then with R_a known, the voltage constant is calculated from Equation (3.2) as:

$$K_v = \frac{N}{V_a} \tag{3.5}$$

where V_a is the effective voltage applied to the armature and N is the motor speed expressed in units of rotations per minute (RPM). This results in a voltage constant with units of RPM/V. Applying Kirchhoff's voltage law [29] to Figure 3.1 and evaluating for the armature voltage yields:

$$K_v = \frac{\omega}{V_{ps} - I_a R_a} \tag{3.6}$$

where V_{ps} and I_a are measured by the multimeter and R_a was calculated using Equation (3.4). The motor speed, N, was determined indirectly with an oscilloscope by measuring the frequency, f, of the waveform at one of the motor leads and then calculating

motor speed as:

$$N = \frac{60f}{N_p/2} \tag{3.7}$$

where N_p is the number of magnetic poles in the motor and $N_p = 14$ for the AXi 4120/18 motors.

The last electrical parameter to be considered is the no-load current, I_0. The no-load current was measured when the nominal armature voltage was applied as indicated by the manufacturer. The no-load current represents the amount of current necessary to overcome losses in the motor and spin the output shaft. Available current in excess of I_0 will then generate torque according to the relationship given in Equation (3.1). As will be shown in Section 3.3, the no-load current is not constant and is included here only for comparison against the specifications.

Equipment used to measure the data necessary to characterize the motors were a Circuit Specialists CSI3005XIII power supply, a Hewlett-Packard 54503A oscilloscope, and an Extech 420 digital multimeter. Table 3.1 compares the experimentally determined motor parameters to those published by the motor manufacturer. As shown, the voltage constant and no-load current are in reasonable agreement while the armature resistance was off by a factor of three. The discrepancy may be due to the fact that the current was measured using a motor current of 5 amps while the motor is rated at, and the manufacturer may have measured at, 40 amps.

3.2 ELECTRONIC SPEED CONTROLLER

A complicating factor with the use of brushless motors is the introduction of an electronic speed controller (ESC), a device external to the motor which electronically performs the commutation achieved mechanically in brushed motors. The ESC converts the battery pack DC voltage to a three phase alternating signal which is synchronized to

Table 3.1: AXi 4120/18 Motor Parameters

Parameter	Symbol	Value	Spec.	Units
Voltage Constant	K_v	523	515	RPM/V
Armature Resistance	R_a	24.2	70	mΩ
No-Load Current (10V)	I_0	1.5	1.5	A

the rotation of the rotor and applied to the armature windings. The motor speed is then proportional to the root-mean-square (RMS) value of the armature voltage and is set by the ESC in response to a pulse width modulated control signal. The relationship between the control signal and the voltage level is not necessarily linear and must be confirmed experimentally. For example, the ESC units used for this quadrotor could be programmed to provide either a linear power response or a linear speed response.
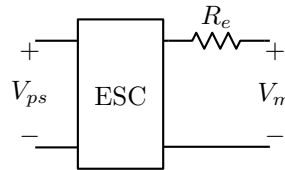
Figure 3.2: Electronic Speed Controller Model

Direct measurement of the three phase voltage or current can be made with a true RMS meter with sufficient bandwidth and current limits only if it is known whether the armature windings are connected in a wye or a delta configuration. An alternate approach is to model the ESC as shown in Figure 3.2. Accounting for the power consumed by the electronics, P_e, the power available to the motor can be determined from the power supply voltage and current as:

$$P_m = V_{ps}I_{ps} - P_e \tag{3.8}$$

Power consumed by the ESC is expected to be negligible under normal operating conditions, however, this loss may be a factor when collecting measurements under low power, such as when calculating motor core loss with no load. Assumed constant, P_e can be determined from Equation (3.8) by applying power to the ESC without connecting the motor leads. The resistor, R_e, shown in Figure 3.2, represents the resistance of the solid state switches and the value is provided by the manufacturer.

An issue encountered with the ESC used for the quadrotor is the presence of an automatic calibration routine that scales the output voltage based on the range of the motor control signal received. During preflight of a fixed wing remote controlled aircraft, the vehicle is restrained while raising the throttle to the maximum value ensuring that the calibration covers the full range of the motor control signal. However, a preflight run-up is not desirable with the quadrotor configuration. In addition, the ESC must be powered up at zero throttle, both for safety considerations and to avoid inadvertently entering an ESC programming mode. As a result, the quadrotor ESC applies a default maximum control signal for which the maximum motor speed occurs at only 55% of the full range. Increasing the throttle to higher levels forces a recalibration, but only after the control signal is reduced back below the initial maximum.

The impact of the automatic recalibration is illustrated in Figure 3.3 where three throttle sweeps were accomplished on an unloaded motor. The initial sweep reflects the default scaling to 55% throttle. Prior to the second sweep the throttle was quickly raised from 55% to maximum and then back to the zero position, resulting in a recalibration with maximum motor speed occurring at 70% throttle position. The process was repeated for the third sweep but this time the throttle was momentarily held at maximum and it resulted in an automatic recalibration that spanned the full range of throttle motion. If all four motors were to simultaneously experience the same recalibration during flight, the result

would be a decrease in thrust that could be compensated for by the operator. On the other hand, dynamic maneuvering near maximum throttle could cause some motors to recalibrate independently of the others, resulting in a dead zone followed by decreased responsiveness for those motors only. This effect must be considered as part of the vehicle stabilization design.
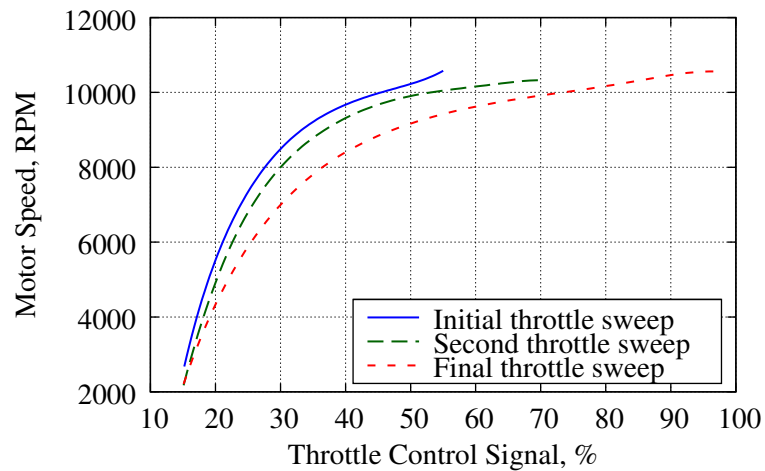
Figure 3.3: Varying throttle response due to ESC auto-calibration

3.3 MODELING CORE LOSS

An improvement over the typical model can be made by accounting for the core loss in the motor. Core loss stems from the heat loss due to eddy currents that are induced in the iron core of the motor and also from the hysteresis of the magnetic field intensity in the core [30]. The core losses are difficult to characterize analytically, as they are a function of the materials used and the physical configuration of the motor. One method to estimate the core loss is to measure the power required to turn the motor without the propeller attached. Neglecting mechanical and copper losses, the power required can then be attributed to core loss [31] and the corresponding no-load current, I_o, can be incorporated into the motor

model as shown in Figure 3.4 [32]. However, this no-load current model is suitable only
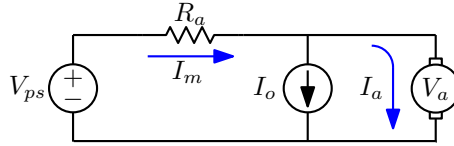
Figure 3.4: No-Load Current Model

for operating speeds near the no-load speed of the motor [31]. As a testbed platform that supports a variety of payload configurations, the takeoff weight of the AEC quadrotor can range from 16.5–26.5 lbs, corresponding to an operating range for the motor of 50–70% of the no-load motor speed. With a wide variation in operating speed, the adequacy of the no-load current model must be considered.

3.3.1 Variation in Core Loss as a Function of Motor Speed

Several models for core loss are available that account for frequency variation. The simplest, the Steinmetz equation, is a nonlinear model that describes core loss as a function of frequency and magnetic flux intensity:

$$P_c = k f^\alpha B_m^\beta \tag{3.9}$$

where f and B_m are the frequency and peak flux density, respectively, for sinusoidal magnetic fields and k, α, and β are constants specific to the magnetic material. The three constants can be empirically matched to data collected in various frequency bands, providing a "fair approximation" to the actual values [33].

A generalization of the Steinmetz equation has been successfully applied to nonsinusoidal signals and might be applicable if the Steinmetz coefficients were known [34]. Other models account separately for the hysteresis and eddy currents. In addition, a third term

can also be introduced to account for residual excess losses. For a nonsinusoidal source, as in the case of a brushless motor, an improved model for specific core loss is [35]:

$$P_c/w = k_{ch}k_h f B_m^\alpha + \frac{k_e}{2\pi^2}\left(\frac{dB}{dt}\right)_{rms}^2 + \frac{k_a}{(2\pi^2)^{\frac{3}{4}}}\left(\frac{dB}{dt}\right)_{rms}^{1.5} \tag{3.10}$$

where k_{ch} is an empirical correction factor for minor hysteresis loops; k_h, k_e, and k_a are the hysteresis, eddy current, and anomalous loss coefficients, respectively; α is a constant determined by the material properties, and W_c is the mass of the core material. Applying this model is complicated by the fact recent research has shown that the anomalous loss term may be superfluous and that the loss coefficients vary as a function of frequency and flux density [36]. In addition, although motors using laminated silicon steel generally are expected to have very small eddy currents [32], rapid changes in the flux density will affect both the eddy current term and the anomalous loss term. In fact, significant pulses in the armature current coinciding with the current switching by the electronic speed controller have been shown to have a large impact on core loss [37].

3.3.2   An Empirical Model for Rotational Loss

Determination of the coefficients in Equation (3.10) is beyond the scope of this project. Instead, an empirical model generated from measured data will be used. Based on the general forms of Equations (3.9) and (3.10) and omitting the anomalous loss term, the rotational loss including the core loss, is expected to have the following relationship:

$$P_r = K_1 N + K_2 N^2 \tag{3.11}$$

where K_1 and K_2 are constants. The procedure used to collect the data necessary to determine these constants is described next.

With no load attached and the control signal to the electronic speed controller increased, the current draw initially rises with the motor speed but quickly reaches a steady-

state value. Data collection to determine the frequency dependence of core loss is therefore primarily concerned with measurements taken for smaller values applied to the control signal. With no load applied, the rotational power loss in the armature, P_r, can be calculated from Figure 3.5 as:

$$P_r = P_{ps} - P_e - I_r^2 R_m \qquad (3.12)$$

where R_m is a composite motor resistance, $R_m = R_a + R_e$, that is defined for convenience, P_{ps} is the power supplied to the electronic speed controller which can be measured directly or calculated as $P_{ps} = I_{ps} V_{ps}$, and I_r is the motor current necessary to overcome the rotational loss. The second term in Equation (3.12) takes into account the copper loss, a term that is expected to be negligible since the no-load armature currents will be small. Also, this method does not distinguish between core loss and mechanical loss as the field in a permanent magnet motor cannot be electrically removed to isolate the mechanical losses. An option, not pursued in this research, is to determine the mechanical losses by using a *dummy* motor in which the permanent magnets have been destructively removed from the rotor [37]. Instead, the rotational loss calculated includes both core and mechanical loss.
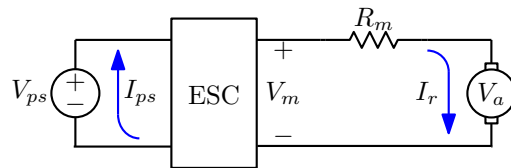
Figure 3.5: ESC and Motor

An alternate expression for the power consumed by the armature is

$$P_r = I_r V_a \qquad (3.13)$$

The motor current can then be calculated by equating the two expression for rotational loss, Equations (3.12) and (3.13)

$$I_r^2 R_m + I_r V_a + (P_e - P_{ps}) = 0 \tag{3.14}$$

Substituting into this equation with Equations (3.2) and (3.8) yields the quadratic equation

$$I_r^2 R_m + I_r \left(\frac{N}{K_v} \right) + (P_e - P_{ps}) = 0 \tag{3.15}$$

where the one solution that is physically realizable represents the armature current required to overcome the core and mechanical loss

$$I_r = \frac{-\frac{N}{K_v} + \sqrt{\left(\frac{N}{K_v} \right)^2 - 4(P_e - P_{ps})R_m}}{2R_m} \tag{3.16}$$

From Equations (3.2) and (3.13), the rotational loss is

$$P_r = I_r N / K_v \tag{3.17}$$

Figure 3.6 shows the difference between the constant no-load current model and the rotational loss data collected. After using regression to determine the model constants, the speed-dependent model presented in Equation (3.11) is found to aptly describe the data collected. For the constant no-load current model depicted, I_o was measured at an applied voltage of 10 V to match the published specification for that motor. Whereas there is a difference between the two models, in the operating region of 5000–7500 RPM, the models are a close match. Furthermore, it will be shown that the rotational losses, which dominate at lower speeds, play a diminishing role at greater speeds. Therefore, the use of the no-load current model is sufficient.

As with the no-load current model, the motor speed is directly proportional to the voltage across the armature so it is sufficient to model the rotational loss in terms of the
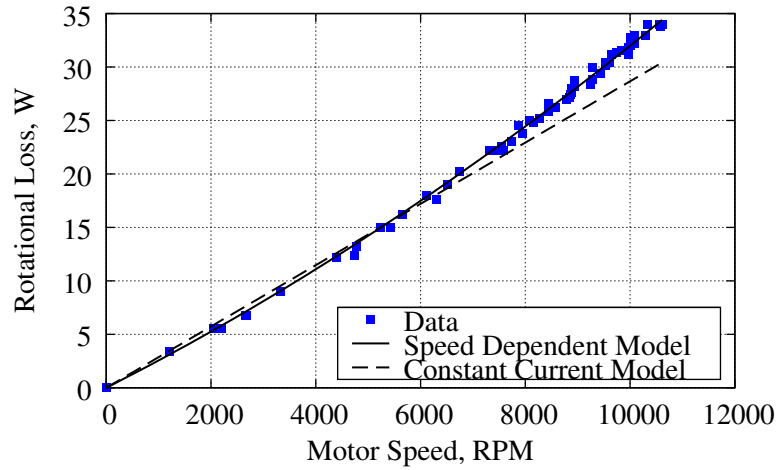
Figure 3.6: Comparison of Rotational Loss Models

associated current, I_r, which can be calculated by dividing the power in Equation (3.11) by the armature voltage from Equation (3.2) to arrive at

$$I_r = K_1 K_v + K_2 K_v N \tag{3.18}$$

This current is then incorporated into the motor model as shown in Figure 3.7.
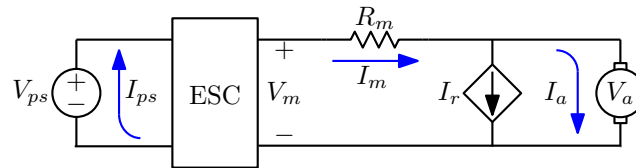
Figure 3.7: Frequency Dependent Core Loss Model

3.4 LITHIUM POLYMER BATTERIES

Lithium Polymer batteries are well suited for the quadrotor due to their high specific energy. These batteries also have a low internal resistance which can be considered negligible for some applications. For high power applications, however, the loss associated

with this resistance, dissipated as heat in the battery pack, accounts for a significant portion of the power budget and must be considered. The impact of the internal resistance is evident in Figure 3.8, which plots data for increasing thrust measurements. The pulse train appearance results from spacing the test points to allow the open circuit battery voltage to approach the resting voltage. The difference between the resting voltage and the voltage under load, ΔV_b, corresponds to the voltage drop across the battery pack's internal resistance,

$$R_b = \Delta V_b / I_b \tag{3.19}$$

where I_b is the measured current under load.
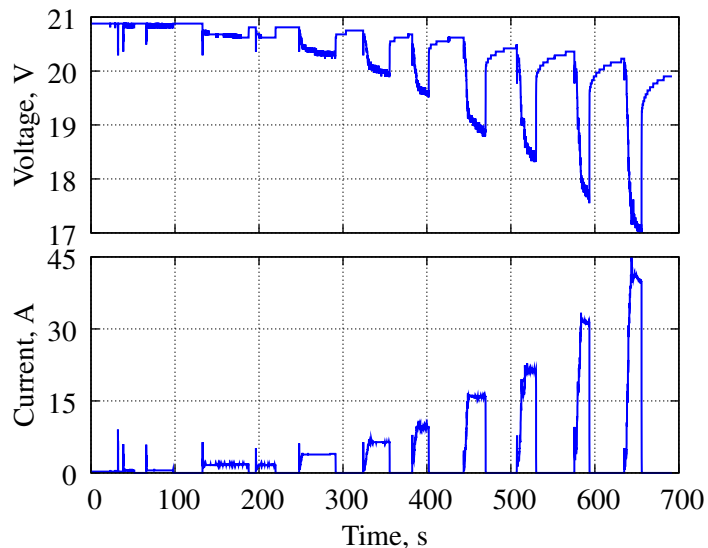
Figure 3.8: Variation in Battery Voltage due to Internal Resistance.

Interestingly, when the internal resistance is plotted as a function of current (see Figure 3.9) the resistance actually decreases with current for moderate to heavy loads experienced in the quadrotor's operating region. This is consistent with an analytical

expression for the internal resistance of a single lithium ion cell [38]

$$R_b = r_1(t) + \frac{r_2(t) \ln I_b}{I_b} + \frac{r_3(t)}{I_b} \tag{3.20}$$

where coefficients r_1, r_2, and r_3 are functions of temperature, t. Although this Ohmic overpotential increases with temperature, the terminal voltage is also limited by the concentration overpotential which decreases with temperature [38]. Ignoring temperature effects, Equation (3.20) can then be used to model the resistance of the quadrotor battery packs using constant coefficients. Note that the model is ill-behaved for small currents but adequately describes the region of interest (see Figure 3.9). Also, the model is somewhat optimistic as the internal resistance will increase as the cells age.
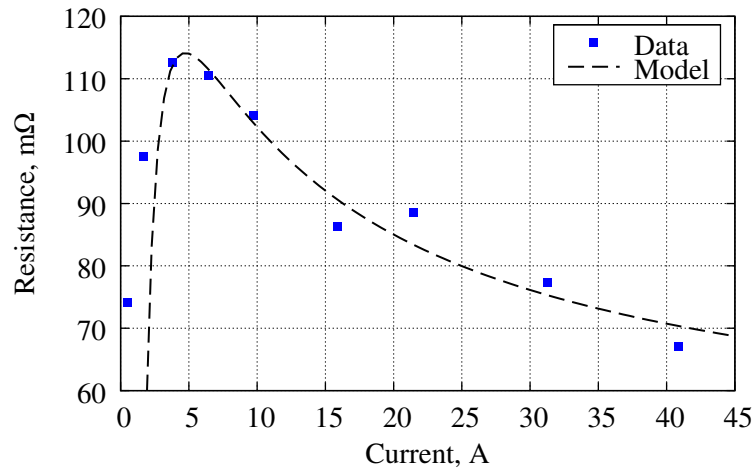
Figure 3.9: Battery pack internal resistance

3.5 PROPELLERS

With four independent rotors, flight control can be established without the use of cyclic pitch and therefore simple fixed pitch propellers can be employed. With rotors arranged in counter-rotating pairs, sets of rotors that are matched in terms of twist and airfoil are

desirable. Fortunately, pusher propellers, normally mounted at the back of a fixed wing aircraft, can be applied since the brushless motors are easily reversed by merely swapping two of the three motor leads. Although selection is limited, large diameter propellers are available in matching pusher and tractor configurations.

Characterization of the propulsion system required measurement of thrust data collected along with the electrical motor parameters. The thrust test stand configuration for this project consisted of a hinged lever with the motor mounted on the free end. A pusher propeller attached to the motor shaft provided a downward directed force that was measured using a digital scale. No special provisions were made to account for the airflow, which limited the maximum thrust that could be measured. At higher throttle settings with an exit velocity of 52 mph, the induced air flow circulated about the room and corrupted the data by impinging on the test stand. Data collected was sufficient to characterize the normal range of operation based on current limits within the motor. Measurements with a larger propeller, without having to rely on an extrapolated model, would require a better ability to control the airflow during the data runs.

A suitable power supply capable of providing nearly a kilowatt of power to drive the motor and propeller was not available. Instead, a five cell lithium polymer battery pack provided the necessary power at a nominal voltage of 18.5 V. Expected current levels exceed the capability of typical laboratory in-line meters, so the battery voltage and current were collected using an Eagle Tree data logger which was placed in line with the battery cable and provided both current and voltage readings. Motor speed was calculated from the frequency of the three-phase voltage measured at one of the motor leads. The relationship of this frequency to the motor speed is:

$$N = \frac{60f}{N_p/2} \tag{3.21}$$

where N_p is the number of magnetic poles in the motor.

Since the data logger provides the terminal voltage on the battery, it is not necessary to account for the internal resistance of the battery and the model shown in Figure 3.7 is sufficient. The current drawn by the motor can be calculated in an analogous manner as for I_r:

$$I_m = \frac{-\frac{N}{K_v} + \sqrt{\left(\frac{N}{K_v}\right)^2 - 4(P_e - P_{ps})R_m}}{2R_m} \tag{3.22}$$

Then, accounting for the current associated with rotational loss, the armature current is:

$$I_a = I_m - I_r \tag{3.23}$$

and the torque on the motor shaft is calculated using Equation (3.1). With the motor speed and shaft torque known, nondimensional thrust and torque coefficients for the propeller can be determined using [39]:

$$C_T = \frac{T}{\rho\pi R^4\Omega^2} \tag{3.24}$$

$$C_Q = \frac{Q}{\rho\pi R^5\Omega^2} \tag{3.25}$$

Whereas the thrust and torque coefficients vary with the ratio of the free stream velocity to the propeller speed, in a constant altitude hover the free steam velocity is zero and the two coefficients can be approximated as constants. As a sensor testbed, the flight profiles for the AEC quadrotor are expected to be benign with only limited deviations from the hover. As a result the thrust and torque can be modeled as proportional to the square of the motor speed and the coefficients can be determined using regression.

3.6 Inertial Sensor

The Microstrain 3DM-GX1, Figure 3.10, is a MEMS inertial unit capable of providing orientation information using an RS-232 serial port interface. The attitude solution benefits greatly from the application of a Microstrain proprietary algorithm that blends the output

of orthogonal gyroscopes with data from the accelerometers and magnetometers in order to minimize drift and sensitivity to inertial forces. For dynamic applications, the 3DM-GX1 typically provides two degree RMS accuracy [40]. Their level of performance and their relative low cost makes devices such as these well-suited for unmanned vehicles applications especially when aided by the global positioning system [24, 41, 42]. In addition, without aiding, the 3DM-GX1 has been demonstrated to be capable of hovering a micro-air vehicle autonomously for 35 seconds and for several minutes when assisted by a pilot [43].

Figure 3.10: 3DM-GX1 Orientation Sensor

3.6.1 Limitations

One limitation of the 3DM-GX1 is the sensitivity of the unit's magnetometers to electromagnetic interference and the presence of metal objects. In fact, the magnetic disturbances measured by the 3DM-GX1 have been used as an additional means of positioning [44]. Potential sources of interference on the AEC quadrotor include four high power motors, with motor currents as high as 55 amps each, the avionics associated with the flight control system, and possibly the sensor payload as well. One means of mitigating the errors on the blended navigation solution used for wheeled robots is to position the sensor as far as possible from the sources of interference [45]. Within the

constraints of a small aerial vehicle, an alternate solution is to limit aiding performed by the the magnetometers. For example, German researchers integrating a GPS receiver with a MEMS inertial measurement unit opted to restrict the magnetometers aiding to the yaw channel only where errors such as 20 degrees were considered "tolerable" [42].

In addition to interference, the filtering operation itself can add undesired artifacts. For example, the low pass filter used in the blending algorithm is sensitive to "sustained inertial influences, such as long duration (30 seconds) coordinated turns at velocity", leading an increase in error during the maneuver [46]. Also, the filter adds unspecified phase lag which has a destabilizing effect.

3.6.2 Implementation

To mitigate the interference and eliminate uncertainty associated with the Microstrain proprietary algorithm, the proposed solution is to bypass the proprietary filters altogether and to perform the bias correction and attitude calculation externally in real-time on a field programmable gate array (FPGA). This approach relies solely on the gyroscopes for inertial data, minimizing the impact of electromagnetic interference, and allows implementation on a single light-weight board which is capable of hosting both the attitude algorithm and the flight control system. The remaining sections in this paper detail the implementation of the attitude algorithm, characterize the performance, and present the results noted during flight test of the AEC quadrotor sensor testbed.

Without requiring data from the accelerometers and magnetometers, only a portion of the functionality of the 3DM-GX1 was utilized. As such, this technique could also be applied to discrete microelectromechanical system (MEMS) gyroscopes. However, the 3DM-GX1 sensor package was advantageous because of the digital interface and the gyroscope calibration. The *instantaneous* angular rate vector, to which blending has not

been applied, is compensated for temperature, alignment, and G-sensitivity but not for the constant bias [47].

A byproduct of bypassing the internal bias correction algorithm is an increase in maximum data rate for Euler angles from 100 Hz to 333 Hz [48]. The increased data rate benefits the fidelity of the attitude solution, though the control loop for the quadrotor is still constrained to 50 Hz by the pulse width modulated protocol used by the radio receiver and electronic speed controllers.

3.6.3 Allan Variance Analysis

The instantaneous angular rates retain a significant bias that can be removed by averaging the angular rate during an initialization period and then subtracting this bias from subsequent measurements. The appropriate averaging interval is determined from a plot of the Allan variance versus averaging interval. The Allan variance provides the variation between mean values calculated for consecutive intervals. Based on N_s samples, the Allan variance is calculated as [49]

$$\sigma_A^2(\tau) = \frac{1}{2(K-1)} \sum_{k=1}^{K-1} (\bar{\omega}_{k+1}(N_\tau) - \bar{\omega}_k(N_\tau))^2 \qquad (3.26)$$

where N_τ is the number of sample points in an interval and $K = \text{floor}(N_s/N_\tau)$ is the integer number of distinct intervals that can be formed within the collected data. With data collected at a constant frequency, f, the length of the interval is given by $\tau = N_\tau/f$. The mean value of the kth interval is denoted by $\bar{\omega}_k$.

The percent error associated with the root Allan variance, or Allan standard deviation, is given by [49]

$$\% \text{ error} = \frac{100}{\sqrt{2(K-1)}} \qquad (3.27)$$

Because the percent error grows rapidly as the interval length approaches the sample length, care must be taken to collect sufficient data to avoid erroneous results. The data

set represented in Figure 3.11 was collected at 333 Hz from a stationary platform for 6.7 hours and exhibits less than ten percent error for averaging intervals under eight minutes in length. The minimum point for each curve indicates the interval length for which the calculated mean will remove the bias with minimal residual error. Although the three gyros attained minimum variance at different interval lengths, for simplicity a single initialization period of 50 seconds was selected for all three gyros.
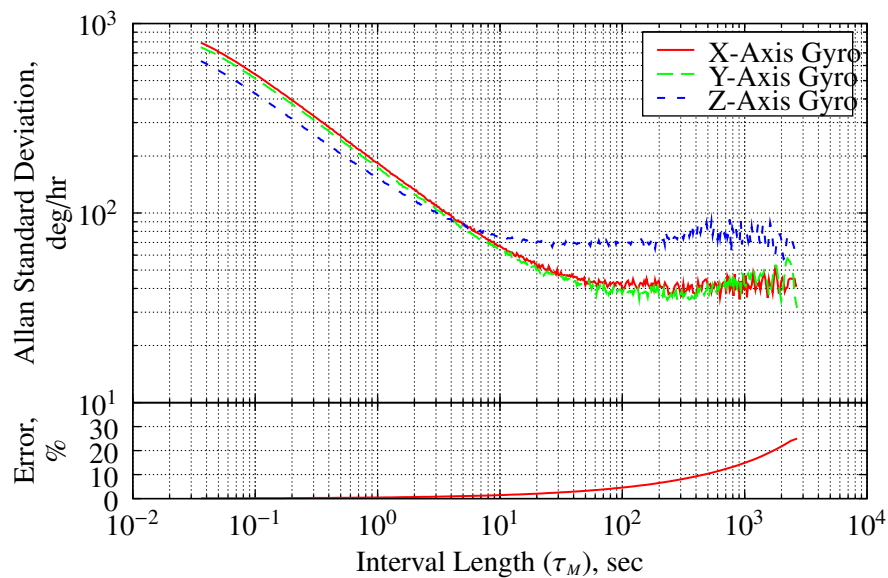
Figure 3.11: Allan Variance Plot for the Gyroscopes

The Allan variance analysis also provides a graphical method for estimating sensor noise based on the slopes of various line segments as detailed in references 49 and 50. In particular for the quadrotor, the slope of -0.5 for short averaging intervals is indicative of angle random walk and the level segment for longer intervals is associated with the bias instability. The expression for the angle random walk coefficient is typically presented as [49]

$$\sigma_A = \frac{A^2}{\tau} \tag{3.28}$$

which requires one to extrapolate the sloped line to an intercept point at $\tau = 3600$ seconds. Adding a conversion factor results in an expression that can be applied directly to the curve as depicted

$$A = \sigma_A \frac{\sqrt{\tau}}{60} \tag{3.29}$$

As an example, for the x-axis gyroscope shown in Figure 3.11, the standard deviation for a 0.85 sec interval is 200 deg/hr corresponding to a angle random walk of 3.1 deg/$\sqrt{hr}$. The bias instability coefficient, B, is proportional to Allan standard deviation of the horizontal segment [49]

$$B = \sigma_A \sqrt{\frac{\pi}{2 \ln 2}} \tag{3.30}$$

The noise coefficients extracted from the Allan variance analysis are listed in Table 3.2 for each of the three gyroscopes. The measured coefficients are found to be in reasonable agreement with the specifications provided by the manufacturer, though the z-axis gyroscope exhibits a larger than expected bias instability.

Table 3.2: Allan Variance-Derived Noise Coefficients

Noise Source	Units	Spec.	Value	
Angle Random Walk	$\dfrac{deg}{\sqrt{hr}}$	3.5	x-axis	3.1
			y-axis	2.9
			z-axis	2.6
Bias Instability	$\dfrac{deg}{hr}$	72	x-axis	61
			y-axis	56
			z-axis	104

4   Aerodynamic Model

This chapter is laid out as follows. First, the notation is introduced in Section 4.1. Next, the nonlinear equations of motion are derived for the rigid body. Then the gyroscopic effects of the four spinning motors are modeled. Finally, the external forces and moments are included and the equations linearized in Section 4.6

4.1   Notation

This dissertation adopts a symbol notation that is typical of that used in aerodynamic texts. Each vector in this body reference frame can be described in terms of its components along each axis. The velocity vector is then composed of three components, u, v, and w, that lie along the x, y, and z axes, respectively. Likewise, angular velocity is comprised of p, q, and r components, the total moment is comprised of L, M, and N components, and the total force has F_x, F_y, and F_z components along the same axes. Finally, the total moment of inertia is expressed with components along each axis, I_x, I_y, and I_z, with the associated products of inertia being I_{xy}, I_{yz}, and I_{xz}. This notation is summarized in Table 4.1.

Table 4.1: Notation Used for the Aerodynamic Model

Axis	Velocity	Angular Rate	Moment	Moment of Inertia	Force
x	u	p	L	I_x	F_x
y	v	q	M	I_y	F_y
z	w	r	N	I_z	F_z

Engineering units will be employed in this dissertation as is standard for the subject of aerodynamics in the United States. To review, in the English system, a *slug* represents a

unit of mass and *pound* is represents a unit of force. This is contrary to the common use of the term *pound* as a mass analogous to the kilogram in the meter-kilogram-second (MKS) system.

4.2   MASS PROPERTIES

Mass properties of interest for the quadrotor are the total mass, *m*, the location of the center of gravity (CG), and the various products of inertia. Based on the two planes of symmetry and neglecting the electrical components mounted on top of the vehicle, a first-order approximation would locate the center of gravity along the *z*-axis and would establish the product of inertias to be zero. Furthermore, one would expect from the design that $I_x \approx I_y$. However, the magnitudes of the moment of inertias are required to model the equations of motion and the vertical location of the CG is required to align the quadrotor's axis of rotation with the two degree of freedom test fixture. Without the ability to perform an experimental weight and balance, the technique used in the research was to model the mass distribution of individual components to an acceptable level of fidelity and then to analytically calculate the mass properties of the overall quadrotor.

As the mass properties for the quadrotor are dominated by the heavier components, some lesser components, such as wires or fasteners were neglected outright with the knowledge that their light weight would have negligible contributions to the total mass and inertia. Other lighter components were combined with a heavier component which accounted for the mass of the lesser component but distributed this mass over the rectangular prism that approximates the volume of the heavier component. The procedure for calculating the mass properties follows.

4.2.1 Center of Gravity

First, for a specific component, i, the mass of that component, m^i was measured using a digital scale. The total mass was then calculated as:

$$m = \sum_i m^i \qquad (4.1)$$

Next the component was modeled by a rectangular prism encompassing nearly the same volume and rough dimensions as the actual component. For convenience, the prism was chosen such that the sides aligned with the axis of the body reference frame. Initially, the origin of the body frame was positioned at the top center of the cross-frame structure, and the axes were denoted x', y', and z'. Each component's location in the initial body frame is then specified completely by two endpoints on each axis. For example, the two x-axis endpoints for the ith component are $x_0'^i$ and x_1' with $x_0' < x_1'$ by definition. Table 4.2 lists each component in the initial flight configuration with its total mass and the opposing corners of the prism that approximates the component volume. Table 4.3 lists the carbon fiber sub-frame and payload components that were flown in subsequent flights.

With an assumed uniform density for the component model, the component center of gravity, CG^i, is centered in the box and:

$$
\begin{aligned}
CG^i_{x'} &= x_0'^i + \frac{\Delta x^i}{2} & & & \Delta x^i &= x_1'^i - x_0'^i \\[2mm]
CG^i_{y'} &= y_0'^i + \frac{\Delta y^i}{2} & \text{where} & & \Delta y^i &= y_1'^i - y_0'^i \\[2mm]
CG^i_{z'} &= z_0'^i + \frac{\Delta z^i}{2} & & & \Delta z^i &= z_1'^i - z_0'^i
\end{aligned}
\qquad (4.2)
$$

Table 4.2: Component Mass Properties - Initial Configuration

Component	Mass (lb)	First Corner (in)			Opposing Corner (in)		
		x	y	z	x	y	z
Boom 1	0.34	0.25	15	−0.5	0.5	−1	0
Boom 2	0.34	−0.5	0.5	0.25	15	−1	0
Boom 3	0.34	−15	−0.25	−0.5	0.5	−1	0
Boom 4	0.34	−0.5	0.5	−15	−0.25	−1	0
Chassis	1.98	−6	6	−6	6	0	2.75
Battery Foam	0.41	−6	6	−6	6	0	2.75
Battery 1	1.75	1	3.5	−5	5	1.38	2.38
Battery 2	1.75	−3.5	−1	−5	5	1.38	2.38
Battery 3	1.75	−5	5	1	3.5	0.38	1.38
Battery 4	1.75	−5	5	−3.5	−1	0.38	1.38
Motor/Prop 1	0.98	13	15	−1	1	0	3.75
Motor/Prop 2	0.98	−1	1	13	15	0	3.75
Motor/Prop 3	0.98	−15	−13	−1	1	0	3.75
Motor/Prop 4	0.98	−1	1	−15	−13	0	3.75
ESC 1	0.15	6.5	9.25	0.5	1	−1	0
ESC 2	0.15	−1	−0.5	6.5	9.25	−1	0
ESC 3	0.15	−9.25	−6.5	−0.5	−1	−1	0
ESC 4	0.15	0.5	1	−9.25	−6.5	−1	0
FPGA Board	0.34	−2.75	2.75	−1.25	2.75	4.5	5
FPGA Standoff	0.11	−2.75	2.75	−1.25	2.75	3	4.5
Inertial Sensor	0.16	−1.25	1.25	−1.25	1.25	3	4
Radio Receiver	0.07	−5.38	−3.13	−2.94	−1.44	3	3.75
Battery	0.10	1.5	3.5	−3.5	−2.25	3	3.5
Volt. Regulator	0.03	−4.5	−3.5	0.75	2.5	3	3.5

Table 4.3: Component Mass Properties - Payload and Carbon Fiber Sub-Frame

Component	Mass (lb)	First Corner (in)			Opposing Corner (in)		
		x	y	z	x	y	z
Sub Frame	0.42	-7	7	-7	7	-14	0.75
Container	0.29	-2	2	-2	2	-5.5	-1
Small Payload	2.85	-2	2	-2	2	-5.5	-4.7
Medium Payload	4.38	-2	2	-2	2	-5.5	-3.33
Large Payload	5.85	-2	2	-2	2	-5.5	-4.13
Max Payload	10.26	-2	2	-2	2	-5.5	-2.25
LD-OEM LADAR	5.40	-2.37	2.37	-2.26	2.26	-9.74	-1

The quadrotor's CG in the initial body frame can be calculated treating each component as a point mass located at the component's CG:

$$CG_{x'} = \frac{1}{m} \sum_i \left(m^i \cdot CG_x^i \right)$$

$$CG_{y'} = \frac{1}{m} \sum_i \left(m^i \cdot CG_y^i \right) \tag{4.3}$$

$$CG_{z'} = \frac{1}{m} \sum_i \left(m^i \cdot CG_z^i \right)$$

Finally, the origin of the body reference frame was adjusted by an amount equal to the offset in the quadrotor's CG. This correction shifts the origin of the body reference to the CG so that the component locations are correctly situated in the true body reference frame

$$x_1 = x_1' - CG_{x'} \qquad y_1 = y_1' - CG_{y'} \qquad z_1 = z_1' - CG_{z'}$$
$$\tag{4.4}$$
$$x_0 = x_0' - CG_{x'} \qquad y_0 = y_0' - CG_{y'} \qquad z_0 = z_0' - CG_{z'}$$

4.2.2 Inertia

With the origin of the body frame correctly established at the CG, the moments and products of inertia in the body frame are defined as

$$
I_x = \iiint\limits_{V} \left(y^2 + z^2 \right) dm \qquad\qquad I_{xy} = \iiint\limits_{V} (xy)\, dm
$$

$$
I_y = \iiint\limits_{V} \left(x^2 + z^2 \right) dm \qquad\qquad I_{yz} = \iiint\limits_{V} (yz)\, dm \qquad (4.5)
$$

$$
I_z = \iiint\limits_{V} \left(x^2 + y^2 \right) dm \qquad\qquad I_{xz} = \iiint\limits_{V} (xz)\, dm
$$

where the inertias are integrated over the component volume and

$$
dm = \frac{m}{\Delta x \Delta y \Delta z} \qquad (4.6)
$$

With each component modeled as a box with sides that are aligned with the body axes, the equations reduce in a straight-forward manner to

$$
I_x = \frac{m}{3}\left(\frac{y_1^3 - y_0^3}{\Delta y} + \frac{z_1^3 - z_0^3}{\Delta z} \right) \qquad\qquad I_{xy} = \frac{m}{4}\left(\frac{y_1^2 - y_0^2}{\Delta y} \times \frac{z_1^2 - z_0^2}{\Delta z} \right)
$$

$$
I_y = \frac{m}{3}\left(\frac{x_1^3 - x_0^3}{\Delta x} + \frac{z_1^3 - z_0^3}{\Delta z} \right) \qquad\qquad I_{yz} = \frac{m}{4}\left(\frac{x_1^2 - x_0^2}{\Delta x} \times \frac{z_1^2 - z_0^2}{\Delta z} \right) \qquad (4.7)
$$

$$
I_z = \frac{m}{3}\left(\frac{x_1^3 - x_0^3}{\Delta x} + \frac{y_1^3 - y_0^3}{\Delta y} \right) \qquad\qquad I_{xz} = \frac{m}{4}\left(\frac{x_1^2 - x_0^2}{\Delta x} \times \frac{y_1^2 - y_0^2}{\Delta y} \right)
$$

Based on the component models listed in Table 4.2, the quadrotor mass properties are summarized in Table 4.4.

4.3 RIGID BODY DYNAMICS

A analytical model for the quadrotor can be developed from the equations of motion for a rigid body, which relate internal and external forces and moments using Newton's second law. The basic equations of motion are readily available [51, 52], and the model

Table 4.4: Quadrotor Mass Properties

Property	Value	Units
Center of Gravity Offset		
x'-axis	-1.21×10^{-2}	in
y'-axis	-3.40×10^{-3}	in
z'-axis	1.18×10^{0}	in
Moments of Inertia		
I_x	1.21×10^{-1}	slug $\cdot$ ft^2
I_y	1.21×10^{-1}	slug $\cdot$ ft^2
I_z	2.32×10^{-1}	slug $\cdot$ ft^2
Products of Inertia		
I_{xy}	6.26×10^{-5}	slug $\cdot$ ft^2
I_{yz}	-9.52×10^{-5}	slug $\cdot$ ft^2
I_{xz}	-5.35×10^{-5}	slug $\cdot$ ft^2

development for the quadrotor will start with Equations (4.8) and (4.9) for the forces and moments, respectively. Note that in each force equations, the expected $F = ma$ term is supplemented by two products. The additional terms arise due to the fact that the aircraft body axis may be rotating with respect to inertial space. Likewise, the moment equations carry a number of additional terms related to aircraft rotation.

$$F_x = m(\dot{u} + qw - rv)$$
$$F_y = m(\dot{v} + ru - pw)$$
$$F_z = m(\dot{w} + pv - qu)$$

(4.8)

$$L = I_x\dot{p} - I_{xy}\dot{q} - I_{xz}\dot{r} - I_{xz}pq - I_{yz}q^2 + (I_z - I_y)qr + I_{xy}pr + Iyzr^2$$

$$M = -I_{xy}\dot{p} + I_y\dot{q} - I_{yz}\dot{r} + (I_x - I_z)pr - I_{xy}qr + I_{xz}(p^2 - r^2) + I_{yz}pq \quad (4.9)$$

$$N = -I_{xz}\dot{p} - I_{yz}\dot{q} + I_z\dot{r} - I_{xy}p^2 + (I_y - I_x)pq - I_{yz}pr + I_{xy}q^2 + I_{xz}qr$$

By orienting the body frame with the cross-frame, the symmetrical design of the quadrotor can be exploited to reduce the number of terms in the moment equations. Specifically, because of the symmetry across the x-z plane, I_{yz} and I_{xy} can be neglected, as shown in Table 4.4 where they are four orders of magnitude less than the moments of inertia.[1] This results in the familiar form used for airplanes, which have only one plane of symmetry:

$$L = I_x\dot{p} - I_{xz}\dot{r} + (I_z - I_y)qr - I_{xz}pq$$

$$M = I_y\dot{q} + (I_x - I_z)pr + I_{xz}(p^2 - r^2) \quad (4.10)$$

$$N = -I_{xz}\dot{p} + I_z\dot{r} + (I_y - I_x)pq + I_{xz}qr$$

Because the quadrotor is also symmetric across the y-z plane, I_{xz} is also negligible and the mass distributions about the x and y axis are nearly equal. Therefore, $I_x \approx I_y$ and $I_{xz} \approx 0$, as supported by the values in Table 4.4, so that the moment equations simplify to:

$$L = I_x\dot{p} + (I_z - I_y)qr$$

$$M = I_y\dot{q} + (I_x - I_z)pr \quad (4.11)$$

$$N = I_z\dot{r}$$

4.4 GYROSCOPIC MOMENTS

The development in the preceding section hinges on the assumption of a rigid body aircraft, neglecting the rotation of the motors. The derivation also presupposed that the body maintains a constant mass. With an all electric propulsion system, the latter

---

[1]The symmetry is spoiled by the electronics mounted on the top of the quadrotor, but their mass is relatively small and their influence on the inertia negligible

assumption is valid. The rigid body assumption, however, requires more consideration. Even for a traditional airplane, neglecting the rotating engine components can have disastrous consequences at higher angles of attack where reduced aerodynamic moments can be overwhelmed by the gyroscopic moments [53].

Because the quadrotor operates at relatively slow speeds, the gyroscopic effects of the four spinning motors can be significant. In fact, the torque generated by the motors provides the sole means to yaw the vehicle. Therefore, the gyroscopic moments are appended to the moment equations [53]:

$$
\begin{aligned}
L &= I_x \dot{p} + (I_z - I_y)qr + \dot{H}_x + H_z q - H_y r \\
M &= I_y \dot{q} + (I_x - I_z)pr + \dot{H}_y + H_x r - H_z p \\
N &= I_z \dot{r} + \dot{H}_z + H_y p - H_x q
\end{aligned}
\tag{4.12}
$$

where H represents the total angular momentum of the four motors and

$$
H_x = \sum_{i=1}^{4} I_x^i \omega_x^i \qquad H_y = \sum_{i=1}^{4} I_x^i \omega_y^i \qquad H_z = \sum_{i=1}^{4} I_x^i \omega_z^i \tag{4.13}
$$

where I^i and ω^i are the inertia and angular rate of the ith motor. Because the motor shaft is physically aligned with the z-axis, the motor angular momentum is limited to the z-axis and $\omega_x = \omega_y = 0$. Also, recalling that torque equals the time rate of change of angular momentum, the equations of motion with gyroscopic moments reduce to:

$$
\begin{aligned}
L &= I_x \dot{p} + (I_z - I_y)qr + H_z q \\
M &= I_y \dot{q} + (I_x - I_z)pr - H_z p \\
N &= I_z \dot{r} + Q
\end{aligned}
\tag{4.14}
$$

where motor torque, Q^i, is limited to the z-axis and

$$
Q = \sum_{i=1}^{4} Q^i \tag{4.15}
$$

4.5 EXTERNAL FORCES

Three external forces influence the equations of motion and need to be added to the equations developed thus far. These are the forces due to gravity, thrust, and aerodynamics respectively.

4.5.1 Gravity

First consider the force due to gravity, $\boldsymbol{F}_g$. In the navigation frame, the z-axis is defined to be in the direction of the local gravity vector. In other words, if g is the magnitude of the gravity vector, then:

$$\boldsymbol{F}_g^{\,n} = \begin{bmatrix} 0 & 0 & mg \end{bmatrix}^T \tag{4.16}$$

which can be rotated into the body frame:

$$\boldsymbol{F}_g^{\,b} = \boldsymbol{C}_n^b \boldsymbol{F}_g^{\,n}$$

$$= \begin{bmatrix} \cos\theta\cos\psi & \cos\theta\sin\psi & -\sin\theta \\[2mm] \begin{array}{c} \sin\phi\sin\theta\cos\psi \\ -\cos\theta\sin\psi \end{array} & \begin{array}{c} \sin\phi\sin\theta\sin\psi \\ +\cos\theta\cos\psi \end{array} & \sin\phi\cos\theta \\[2mm] \begin{array}{c} \cos\phi\sin\theta\cos\psi \\ +\sin\phi\sin\psi \end{array} & \begin{array}{c} \cos\phi\sin\theta\sin\psi \\ -\sin\phi\cos\psi \end{array} & \cos\phi\cos\theta \end{bmatrix} \begin{bmatrix} 0 \\ 0 \\ mg \end{bmatrix} \tag{4.17}$$

$$= \begin{bmatrix} -mg\sin\theta \\ mg\sin\phi\cos\theta \\ mg\cos\phi\cos\theta \end{bmatrix}$$

Because the force of gravity pulls equally on the entire mass of the quadrotor, it can be regarded as a single force directed through the vehicle center of gravity. Therefore, there are no moment terms associated with gravity.

4.5.2 Thrust

The line of action of the thrust, $\boldsymbol{T}$, on the other hand, is directed through the center of the rotor disk and aligned with the motor shaft. Each rotor disk will then have a moment arm, $l_m = 14$ (inches) and will therefore generate moments about the center of gravity as well. For modeling purposes, the motors are numbered sequentially from 1–4 starting at the positive x-axis motor and rotating about the z-axis. Also, because the motor shafts are aligned with the z-axis, the x and y components of thrust are zero as is the moment about the z-axis. The components of thrust in terms of forces and moments are

$$
\begin{aligned}
\boldsymbol{T}_x &= 0 & \boldsymbol{L}_T &= l_m\,(T_4 - T_2) \\
\boldsymbol{T}_y &= 0 & \boldsymbol{M}_T &= l_m\,(T_1 - T_3) \\
\boldsymbol{T}_z &= T & \boldsymbol{N}_T &= 0
\end{aligned}
\tag{4.18}
$$

where

$$
T = \sum_{i=1}^{4} T^i
\tag{4.19}
$$

4.5.3 Aerodynamic Forces

Finally, the components of the aerodynamic forces are defined to be C_x, C_y, and C_z and for a typical aircraft these forces would be dominated by the lift and drag produced by the wings and other surfaces. Without an airfoil or a lifting body, the quadrotor structure generates no significant lift or induced drag, so the aerodynamic effects are limited to that of parasitic drag. However, the parasitic drag for any aircraft is minimal at slow airspeeds, the velocity regime in which the quadrotor will operate. Without resorting to the unnecessary complexities of wind tunnel testing or computational fluid dynamics, a rough order of magnitude for the parasitic drag can be calculated that shows that the impact is negligible and can thus be ignored.

Drag can be roughly estimated as [54]:

$$D = \frac{1}{2}C_D A_c \rho V^2 \tag{4.20}$$

where C_D is the coefficient of drag, A is the cross-sectional area, ρ represents the air density, and V is the velocity. The coefficient of drag varies greatly with the shape of the object, but for purposes of this analysis an estimate of $C_D = 1.12$ will suffice. The cross-sectional area facing each axis is than estimated as the combined surface area of the cross-frame, battery enclosure and motors, and are determined to be 0.52 ft^2 for the x and y axis and 1.31 ft^2 for the z-axis, respectively. Approximating the total drag as the sum of the three components of drag as a function of the corresponding cross-section and airspeed, and using the air density at the OU airport on a standard day, $\rho = 2.36 \times 10^{-3}$ slug/ft^{-3}, the resulting aerodynamic forces are found to be negligible:

$$
\begin{aligned}
C_x &= 7 \times 10^{-4} \, u^2 \\
C_y &= 7 \times 10^{-4} \, v^2 \\
C_x &= 2 \times 10^{-3} \, w^2
\end{aligned}
\tag{4.21}
$$

Likewise, the aerodynamic moments resulting from the drag caused by the rotating body, will be of the same order of magnitude and can be ignored. Incorporating gravity and thrust, the equations of motion and expressed in terms of accelerations and angular accelerations for the force equations:

$$
\begin{aligned}
\dot{u} &= -qw + rv - g\sin\theta \\
\dot{v} &= -ru + pw + g\cos\theta\sin\phi \\
\dot{w} &= -pv + qu + g\cos\theta\cos\phi - \frac{T}{m}
\end{aligned}
\tag{4.22}
$$

and moment equations, respectively:

$$\dot{p} = \frac{l_m}{I_x} (T_4 - T_2) + \frac{(I_y - I_z)}{I_x} qr - \frac{H_z}{I_x} q$$

$$\dot{q} = \frac{l_m}{I_y} (T_1 - T_3) - \frac{(I_x - I_z)}{I_y} pr + \frac{H_z}{I_y} p \qquad (4.23)$$

$$\dot{r} = -\frac{\Delta Q}{I_z}$$

4.6 Linearized Equations of Motion

With a benign flight profile, the quadrotor's equations of motion can be linearized about a hovering trim point without imposing any undue restrictions. The trim point is defined as airframe level, stationary, and non-rotating such that

$$p_0 = q_0 = r_0 = 0 \qquad\qquad \phi_0 = \theta_0 = \psi_0 = 0$$
$$\qquad\qquad\qquad\qquad (4.24)$$
$$u_0 = v_0 = w_0 = 0 \qquad\qquad T_{1_0} = T_{2_0} = T_{3_0} = T_{4_0} = \frac{m}{4}$$

There are two desirable consequences of using counter-rotating propellers that are matched in the sense that the airfoils are identical but reversed. First, the same motor speed, but with opposing vector directions for the contra-rotating pair, is required from each motor to generate the thrust. Second, since the moments of inertia are constant, the total angular rate, H_z, is zero.

$$H_z = 0 \qquad (4.25)$$

The equations of motion are linearized by performing a Taylor series expansion of the force equations and eliminating the higher order terms for the force equations:

$$\Delta \dot{u} = -w_0 \Delta p - q_0 \Delta w + v_0 \Delta r + r_0 \Delta v - g \cos \theta_0 \Delta \theta$$

$$\Delta \dot{v} = -u_0 \Delta r - r_0 \Delta u + w_0 \Delta p + p_0 \Delta w - g \sin \theta_0 \sin \phi_0 \Delta \theta + g \cos \theta_0 \cos \phi_0 \Delta \phi \qquad (4.26)$$

$$\Delta \dot{w} = -v_0 \Delta p - p_0 \Delta v + u_0 \Delta q + q_0 \Delta u - g \sin \theta_0 \cos \phi_0 \Delta \theta - g \cos \theta_0 \sin \phi_0 \Delta \phi - \frac{\Delta T}{m}$$

Similarly for the moment equations:

$$\Delta\dot{p} = \frac{l_m}{I_x}(\Delta T_4 - \Delta T_2) + \frac{(I_y - I_z)}{I_x}(r_0\Delta q + q_0\Delta r)$$

$$\Delta\dot{q} = \frac{l_m}{I_y}(\Delta T_1 - \Delta T_3) - \frac{(I_x - I_z)}{I_y}(r_0\Delta p + p_0\Delta r) \tag{4.27}$$

$$\Delta\dot{r} = -\frac{\Delta Q}{I_z}$$

Since the rest of this dissertation will use the linearized equations, the Δ prefix will be dropped for clarity of notation and *all further references to aircraft states are understood to refer to the perturbation states*. Applying the trim conditions specified in Equations (4.24) and (4.25) and expressing the momentum equations in terms of attitude angles instead of angular rates, the linearized equations of motion are summarized as follows:

$$
\begin{aligned}
\dot{u} &= -g\theta & \ddot{\phi} &= \frac{l_m}{I_x}(T_4 - T_2) \\
\dot{v} &= g\phi & \ddot{\theta} &= \frac{l_m}{I_y}(T_1 - T_3) \\
\dot{w} &= \frac{T}{m} & \ddot{\psi} &= -\frac{1}{I_z}Q
\end{aligned}
\tag{4.28}
$$

5 DERIVING ATTITUDE

This chapter introduces three reference coordinate systems for the AEC quadrotor in Section 5.1. The second section then derives platform attitude using a direction cosine matrix implementation.

5.1 REFERENCE FRAMES

There are three reference frames of interest for the AEC quadrotor. Because the inertial sensors that provide angular rates are rigidly attached to the airframe, the first is a body-fixed reference frame, henceforth referred to as the *body frame*. The orientation of the body frame in this dissertation follows that used for an airplane, with the origin located at the center of gravity; the *x*-axis is aligned with one arm, the *z*-axis pointing down, and the *y*-axis aligned with a second arm consistent with a right-hand coordinate system. Note that the distinction between the nose, tail, and wings, as characterized for an airplane, are lost on the quadrotor with two planes of symmetry. As a reference, a blue flag was fixed to one arm to mark the tail.
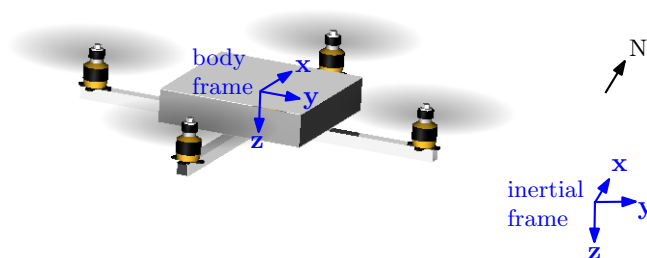

Figure 5.1: Quadrotor Body and Inertial Frames

The second reference coordinate system is the *navigation frame*. The navigation frame is an Earth-fixed reference frame oriented with the *x*, *y*, and *z* axis pointed North, East, and down (NED), respectively, where *down* is defined in terms of the local gravity

vector. Because power limitations restrict the flight profiles to be short in duration and because the AEC quadrotor is flown at low airspeeds, also corresponding to a limited range, the assumptions of a non-rotating, flat Earth are not all restrictive. Therefore, in this dissertation the navigation frame is considered to be in the inertial reference frame.

The third reference frame is used to relate the attitude and position of the quadrotor with respect to the pilot and any sensor targets of interest, generally described in terms of a horizontal position and an altitude. This *target frame* therefore has its axes pointed to the East, North, and up (ENU). The origin of the navigation frame coincides with the origin of the target frame but will be arbitrarily located as required for a specific flight.

All frames have been defined so they represent right-handed coordinate systems. Transformation between these coordinate frames can be performed using direction cosine matrixs (DCMs). In the case of the navigation frame and the target frame, a vector expressed in the navigation frame can be related to a vector expressed in the target frame as follows:

$$\boldsymbol{r}^t = \boldsymbol{C}_n^t \boldsymbol{r}^n \qquad \text{where} \qquad \boldsymbol{C}_n^t = \begin{bmatrix} 0 & 1 & 0 \\ 1 & 0 & 0 \\ 0 & 0 & -1 \end{bmatrix} \qquad (5.1)$$

The superscripts denote the reference frame so that $\boldsymbol{r}^n$ and $\boldsymbol{r}^t$ are vectors in the navigation and target frames, respectively. As $\boldsymbol{C}_n^t$ is a direction cosine matrix, the transpose is used to rotate back the other direction. The relationship between body frames and the navigation frame is slightly more complex and will be discussed in the next section.

5.2 ATTITUDE

The angular relationship between the body and the navigation frames corresponds to the aircraft attitude and can be described using one of three methods: Euler angles, the DCM, and quaternions [55]. Of these, Euler angles will be discussed in Section 5.2.1 and

the direction cosine matrix in Section 5.2.2. The quaternion method is not considered for this dissertation.

5.2.1 Euler Angles

Euler rotation angles are advantageous since they describe the vehicle attitude in a physically meaningful manner. From the navigation frame, the Euler angles, ϕ, θ, and ψ, are applied sequentially about prescribed axes, resulting in a frame oriented with the body axis. The specific sequence of axes used for the Euler angles can vary but must be predefined as rotating about different axes, or even the same axis but in a different order, generally results in different values for the Euler angles. The *yaw-pitch-roll* convention, widely used in the aerodynamic community, is adopted for this dissertation. Taken in the specified order the Euler angles completely specify an aircraft's attitude.

As an example, to find the body attitude, start in alignment with the navigation frame and apply the following three Euler angles: ψ is the heading between the navigation and body x axes found by yawing about the z axis; θ is the pitch angle between the navigation x-y plane and the body x axis found by rotating about the resulting y axis; and ϕ is the roll angle taken about the resulting x axis. Note that the pitch and roll rotations are made from an intermediate frame resulting from the preceding rotation(s). As a result, the Euler angles are functions of the angular rates about these intermediate axis and generally *not* functions of the body axis angular rates. Therefore, the angular rates measured by a strapdown IMU, i.e., non-gimbaled IMU fixed to the body frame, cannot be directly integrated to generate the Euler angles.

An analytical relationship that propagates the Euler angles as a function of the body angular rates can be established [51, 55]:

$$\dot{\phi} = (\omega_y \sin \phi + \omega_z \cos \phi) \tan \theta + \omega_x$$

$$\dot{\theta} = \omega_y \cos \phi - \omega_z \sin \phi \qquad\qquad (5.2)$$

$$\dot{\psi} = (\omega_y \sin \phi + \omega_z \cos \phi) \sec \theta$$

Note that an indeterminate solution occurs at the pitch angles of $90°$ where there is no longer a distinction between roll and yaw angle. In addition, this method relies on trigonometric functions for each update. With an FPGA selected for the implementation of the navigation equations, this necessitates the use of either lookup tables or the coordinate rotation digital computer (CORDIC) algorithm to implement Equation (5.2) [56]. Either option is costly in terms of FPGA resources. In addition, any errors in the trigonometric functions are carried through in the solution. Therefore, a DCM implementation is used from which the Euler angles can be extracted.

5.2.2   Direction Cosine Matrix

The direction cosine matrix (DCM) is a 3×3 matrix which performs a rotation on a vector when it premultiplies that vector. The successive rotations described by the Euler angles are easily calculated as the product of three DCMs taken in the correct order, as shown in Section 5.2.2.1. As will be shown in Section 5.2.2.3, the Euler angles can be extracted from the resulting DCM using three trigonometric functions.

The DCM method is preferred over the direct Euler angle computation because the trigonometric function are used only to extract the angles from the DCM. As a result, an error in a trigonometric function will corrupt the instantaneous attitude but will not impact the attitude solution carried within the DCM. In fact, small angle approximations can

be applied when calculating instantaneous without effecting the accuracy of the attitude maintained within the DCM.

5.2.2.1 Body to Navigation Frame Transformation

If three DCMs are defined to correspond to the Euler angle rotation about each axis:

$$\boldsymbol{C}_{\psi} = \begin{bmatrix} \cos\psi & \sin\psi & 0 \\ -\sin\psi & \cos\psi & 0 \\ 0 & 0 & 1 \end{bmatrix}$$

$$\boldsymbol{C}_{\theta} = \begin{bmatrix} \cos\theta & 0 & -\sin\theta \\ 0 & 1 & 0 \\ \sin\theta & 0 & \cos\theta \end{bmatrix} \tag{5.3}$$

$$\boldsymbol{C}_{\phi} = \begin{bmatrix} 1 & 0 & 0 \\ 0 & \cos\phi & \sin\phi \\ 0 & -\sin\phi & \cos\phi \end{bmatrix}$$

then the total rotation between the navigation frame and the body frame, $\boldsymbol{C}_n^b$, is the product of these three DCMs:

$$\boldsymbol{C}_n^b = \boldsymbol{C}_{\phi}\boldsymbol{C}_{\theta}\boldsymbol{C}_{\psi} = \begin{bmatrix} \cos\theta\cos\psi & \cos\theta\sin\psi & -\sin\theta \\ \begin{aligned}\sin\phi\sin\theta\cos\psi \\ -\cos\theta\sin\psi\end{aligned} & \begin{aligned}\sin\phi\sin\theta\sin\psi \\ +\cos\theta\cos\psi\end{aligned} & \sin\phi\cos\theta \\ \begin{aligned}\cos\phi\sin\theta\cos\psi \\ +\sin\phi\sin\psi\end{aligned} & \begin{aligned}\cos\phi\sin\theta\sin\psi \\ -\sin\phi\cos\psi\end{aligned} & \cos\phi\cos\theta \end{bmatrix} \tag{5.4}$$

Note that matrix multiplication is non-commutative, and so the three matrices must be multiplied in the order specified for the Euler angles, i.e., yaw, pitch and then roll. Also, because the DCM premultiplies the vector to be transformed, the order of the multiplication

in Equation (5.4) runs from right to left, with each successive premultiplication resulting in an intermediate frame, as mentioned in Section 5.2.1.

Although direct application of the Euler angles results in C_n^b, the opposite rotation, transforming from the body frame to the navigation frame is required for navigation. Conveniently, changing the direction of rotation is as easy as taking the transpose of the DCM so that:

$$C_b^n = (C_n^b)^T$$

$$= \begin{bmatrix} \cos\theta\cos\psi & -\cos\theta\sin\psi + \sin\phi\sin\theta\cos\psi & \sin\phi\sin\psi + \cos\phi\sin\theta\cos\psi \\ \cos\theta\sin\psi & \cos\theta\cos\psi + \sin\phi\sin\theta\sin\psi & -\sin\phi\cos\psi + \cos\phi\sin\theta\sin\psi \\ -\sin\theta & \sin\phi\cos\theta & \cos\phi\cos\theta \end{bmatrix} \tag{5.5}$$

5.2.2.2 Propagating C_b^n Through Time

For a strapdown INS, with the inertial sensors rigidly attached to the body as they are in a quadrotor implementation, C_b^n is a critical matrix as it relates the body accelerations and angular rates to the navigation frame. As such, the expressions for propagating C_b^n over time are readily available in texts related to strapdown systems [55, 57]. The development that follows departs from those approaches in that it avoids relying on an unsupported premise, that $C_b^n(t + \Delta t) = C_b^n(t)A(t)$, to reach the solution.

The time derivative of C_n^b is [55]:

$$\dot{C}_b^n = \lim_{\Delta t \to 0} \frac{\Delta C_b^n}{\Delta t} = \lim_{\Delta t \to 0} \frac{C_b^n(t + \Delta t) - C_b^n(t)}{\Delta t} \tag{5.6}$$

where $C_b^n(t + \Delta t)$ describes the rotation between the body frame and the navigation frame at time $t + \Delta t$.

To facilitate the ability to consider rotations of a single frame between two time epochs in time, the notation is modified so that the relevant point in time is explicit in both the superscript and subscript. Hence, this transformation matrix can be substituted by:

$$C_b^n(t + \Delta t) \triangleq C_{b(t+\Delta t)}^{n(t+\Delta t)} \tag{5.7}$$

The right-hand side of Equation (5.7) can be expanded as the product of three rotation matrices:

$$C_{b(t+\Delta t)}^{n(t+\Delta t)} = C_{n(t)}^{n(t+\Delta t)} C_{b(t)}^{n(t)} C_{b(t+\Delta t)}^{b(t)} \tag{5.8}$$

where $C_{n(t)}^{n(t+\Delta t)}$ describes the rotation of the navigation frame over the time increment Δt. Because the navigation frame was chosen to be an inertial reference frame, however, it has no rotation. Hence, this transformation matrix can be substituted by:

$$C_{n(t)}^{n(t+\Delta t)} = I \tag{5.9}$$

and

$$C_{b(t+\Delta t)}^{n(t+\Delta t)} = I C_{b(t)}^{n(t)} C_{b(t+\Delta t)}^{b(t)} \tag{5.10}$$

which reduces to:

$$C_{b(t+\Delta t)}^{n(t+\Delta t)} = C_{b(t)}^{n(t)} C_{b(t+\Delta t)}^{b(t)} \tag{5.11}$$

Simplifying the notation for terms that do not span different time increments improves legibility:

$$C_b^n(t + \Delta t) = C_b^n(t) C_{b(t+\Delta t)}^{b(t)} \tag{5.12}$$

where the rotation matrix, $C_{b(t+\Delta t)}^{b(t)}$, can be derived by first considering its transpose, $C_{b(t)}^{b(t+\Delta t)}$, which rotates the body frame forward in time over the time increment, Δt. If $\Delta\phi$, $\Delta\theta$, and $\Delta\psi$ are the Euler angles describing the incremental rotation, then from Equations (5.3) and

(5.4):

$$
\boldsymbol{C}^{b(t+\Delta t)}_{b(t)} =
\begin{bmatrix}
\cos \Delta\theta \cos \Delta\psi &
\begin{array}{c} \sin \Delta\phi \sin \Delta\theta \cos \Delta\psi \\ - \cos \Delta\theta \sin \Delta\psi \end{array} &
\begin{array}{c} \cos \Delta\phi \sin \Delta\theta \cos \Delta\psi \\ + \sin \Delta\phi \sin \Delta\psi \end{array} \\
\cos \Delta\theta \sin \Delta\psi &
\begin{array}{c} \sin \Delta\phi \sin \Delta\theta \sin \Delta\psi \\ + \cos \Delta\theta \cos \Delta\psi \end{array} &
\begin{array}{c} \cos \Delta\phi \sin \Delta\theta \sin \Delta\psi \\ - \sin \Delta\phi \cos \Delta\psi \end{array} \\
- \sin \Delta\theta & \sin \Delta\phi \cos \Delta\theta & \cos \Delta\phi \cos \Delta\theta
\end{bmatrix}
\tag{5.13}
$$

and the transpose, which conceptually rotates the body frame backwards in time, is equal to:

$$
\boldsymbol{C}^{b(t)}_{b(t+\Delta t)} =
\begin{bmatrix}
\cos \Delta\theta \cos \Delta\psi & \cos \Delta\theta \sin \Delta\psi & - \sin \Delta\theta \\
\begin{array}{c} \sin \Delta\phi \sin \Delta\theta \cos \Delta\psi \\ - \cos \Delta\theta \sin \Delta\psi \end{array} &
\begin{array}{c} \sin \Delta\phi \sin \Delta\theta \sin \Delta\psi \\ + \cos \Delta\theta \cos \Delta\psi \end{array} & \sin \Delta\phi \cos \Delta\theta \\
\begin{array}{c} \cos \Delta\phi \sin \Delta\theta \cos \Delta\psi \\ + \sin \Delta\phi \sin \Delta\psi \end{array} &
\begin{array}{c} \cos \Delta\phi \sin \Delta\theta \sin \Delta\psi \\ - \sin \Delta\phi \cos \Delta\psi \end{array} & \cos \Delta\phi \cos \Delta\theta
\end{bmatrix}
\tag{5.14}
$$

However, $\boldsymbol{C}^{b(t)}_{b(t+\Delta t)}$ is applied in the limit as $t \rightarrow 0$ in Equation (5.6) . Because the Euler angles also approach zero in the limit, small angle approximations can be applied for infinitesimal time increments:

$$
\begin{array}{lll}
\cos \Delta\phi \approx 1 & \sin \Delta\phi \approx \Delta\phi & \Delta\phi \cdot \Delta\theta \approx 0 \\
\cos \Delta\theta \approx 1 & \sin \Delta\theta \approx \Delta\theta & \Delta\theta \cdot \Delta\psi \approx 0 \\
\cos \Delta\psi \approx 1 & \sin \Delta\psi \approx \Delta\psi & \Delta\phi \cdot \Delta\psi \approx 0
\end{array}
\tag{5.15}
$$

so that Equation (5.14) reduces to:

$$
\boldsymbol{C}^{b(t)}_{b(t+\Delta t)} \approx
\begin{bmatrix}
1 & -\Delta\psi & \Delta\theta \\
\Delta\psi & 1 & -\Delta\phi \\
-\Delta\theta & \Delta\phi & 1
\end{bmatrix}
\tag{5.16}
$$

Note that the cross-coupling terms have disappeared, indicating that the order of rotation of the Euler angles is no longer important. As a result, a vector of the incremental Euler angles is equal to the body angular rotation, $\Delta\Theta$, during that time increment:

$$\Delta\Theta = [\Delta\phi \quad \Delta\theta \quad \Delta\psi]^T \tag{5.17}$$

Equation (5.16) can then be rewritten as:

$$C_{b(t+\Delta t)}^{b(t)} = \begin{bmatrix} 0 & -\Delta\psi & \Delta\theta \\ \Delta\psi & 0 & -\Delta\phi \\ -\Delta\theta & \Delta\phi & 0 \end{bmatrix} + I \tag{5.18}$$

$$= \Delta\Theta_\times + I$$

where I is a 3×3 element identity matrix and the subscript $\times$ denotes the skew symmetric cross-product representation of $\Delta\Theta$. Substituting Equations (5.18) and (5.12) back into Equation (5.6) gives:

$$\dot{C}_b^n = \lim_{\Delta t \to 0} \frac{C_b^n(t)(\Delta\Theta_\times + I) - C_b^n(t)}{\Delta t} \tag{5.19}$$

which reduces to:

$$\dot{C}_b^n = \lim_{\Delta t \to 0} \frac{C_b^n(t)\Delta\Theta_\times}{\Delta t} \tag{5.20}$$

Since $C_b^n(t)$ is not a function of Δt:

$$\dot{C}_b^n = C_b^n(t) \lim_{\Delta t \to 0} \frac{\Delta\Theta_\times}{\Delta t} \tag{5.21}$$

Distributing $\frac{1}{\Delta t}$ and applying the limit yields:

$$\dot{C}_b^n = C_b^n(t) \begin{bmatrix} 0 & \lim_{\Delta t \to 0} \frac{-\Delta\psi}{\Delta t} & \lim_{\Delta t \to 0} \frac{\Delta\theta}{\Delta t} \\ \lim_{\Delta t \to 0} \frac{\Delta\psi}{\Delta t} & 0 & \lim_{\Delta t \to 0} \frac{-\Delta\phi}{\Delta t} \\ \lim_{\Delta t \to 0} \frac{-\Delta\theta}{\Delta t} & \lim_{\Delta t \to 0} \frac{\Delta\phi}{\Delta t} & 0 \end{bmatrix} \tag{5.22}$$

and since the time derivative of the body angular rotations is the body angular rate:

$$\dot{C}_b^n = C_b^n(t) \begin{bmatrix} 0 & -\omega_z & \omega_y \\ \omega_z & 0 & -\omega_x \\ -\omega_y & \omega_x & 0 \end{bmatrix} \tag{5.23}$$

where ω_x, ω_y, and ω_z are the components of the body angular rate $\mathbf{\Omega}$ arranged in the skew symmetric cross-product form. Using the cross-product notation, the time derivative of the body-to-navigation rotation matrix is:

$$\dot{C}_b^n = C_b^n(t)\mathbf{\Omega}_\times \tag{5.24}$$

The discrete time equivalent of the attitude propagation, Equation (5.24), is [55]:

$$C_b^n(k+1) = C_b^n(k)e^{\int \mathbf{\Omega}_\times dt} \tag{5.25}$$

Because the gyroscope data rate is high compared to the bandwidth for the quadrotor platform motion, a first-order approximation is sufficient to propagate the attitude direction cosine matrix in discrete time:

$$C_b^n(k+1) \approx C_b^n(k)(I + \mathbf{\Theta}_\times) \tag{5.26}$$

where $\mathbf{\Theta}_\times$ is the skew-symmetric form of the angle vector calculated as:

$$\mathbf{\Theta}_\times = \mathbf{\Omega}_\times \Delta t \tag{5.27}$$

5.2.2.3 Extracting Attitude From C_n^b

If the initial attitude is set using Equation (5.4), then the attitude can be tracked by propagating C_b^n through time with Equation (5.24). For any instance in time, it is possible

to extract the vehicle attitude from C_b^n using the following relationships:

$$\phi = \arctan \frac{C_b^n(3, 2)}{C_b^n(3, 3)}$$

$$\theta = -\arcsin C_b^n(3, 1) \tag{5.28}$$

$$\psi = \arctan2 \frac{C_b^n(2, 1)}{C_b^n(1, 1)}$$

6 FLIGHT CONTROL SYSTEM

6.1 BACKGROUND

Due to the unusual configuration, many exotic control theories have been applied to the quadrotor platform, to include H_∞ controllers [58], a "nested saturation algorithm" [59], robust control using a disturbance observer [60], and non-linear control using back-stepping techniques [21]. Vision based systems have also been used to control the platform using a ground based camera for feedback [23, 61].

Isolating those theories that have been subjected to actual flight tests versus those that were validated in simulation only is insightful. Of those that have been demonstrated to provide sufficient control, several are based on classical control theories. For instance, researchers at the Swiss Federal Institute of Technology compared optimal linear quadratic (LQ) control to classical proportional-integral-derivative (PID) control applied to their OS-4 quadrotor. The control laws were implemented on a separate Linux-based computer and fed back to the quadrotor, presumably, through the same umbilical that was used to provide power. The results were that the "quadrotor can be controlled efficiently in hover using a classical approach" whereas with the LQ controller they were "not able to release the OS4 for a free flight" [62].

In a second example, the Australian X4-Flyer project has also demonstrated that a double lead compensator placed inside a single feedback loop gave "suitable control performance for the pilot augmentation control system." Note that a second feedback loop based on attitude angle was planned but omitted from the test flights because accurate angle measurements were "difficult to obtain" [16]. Similar results were reported for the Korean calamity observation quadrotor which was controlled using PID control with model following for disturbance rejection [23].

6.2 DESIGN GOALS

The goal of the project was to provide a stabilized platform that could be easily flown remotely and not necessarily flown autonomously. Without additional aiding, the gyro drift errors preclude the vehicle from maintaining an absolute position without corrections from the pilot. The control laws are formulated based on a commanded angle for pitch and roll and an angular rate for the yaw channel. For example, the right stick is used to command a bank or pitch angle on the quadrotor where one might expect to command a roll or pitch rate for a typical helicopter. As a result, releasing the stick (spring-loaded to the center) will theoretically cause the aircraft to return to a hover. This implementation is significant in that it lends itself more suitable for control by the novice pilot and also matches the quadrotor role as a sensor platform in that the control is tied directly to the pointing angles that one might desire to achieve.

Performance bounds were qualitatively defined as follows. First, the quadrotor must be cable of flying in calm and low turbulence conditions. Second, the quadrotor will be flown remotely at all times, therefore autonomous flight is not required. Third, since the quadrotor maneuvers only after changing attitude to tilt the lift vector in the desired direction, the FCS is designed to set attitude rather than position. Note that commercial autopilots are available. However, because they rely on the Global Positioning System (GPS) [63], they are not suitable for AEC research involving GPS-denied environments.

6.3 GENERAL METHODOLOGY

Stabilization is accomplished using classical control theory, as shown in the block diagrams for the pitch and yaw channels. Due to symmetry, the roll channel feedback loops and response are identical to the pitch channel. Inner loop feedback from rate gyroscopes provides damping about all three axis and a lead compensated outer feedback loop for the

pitch and roll channels provides the desired attitude tracking. The control loops operate at 50 Hz, corresponding to the frequency of the pulse width modulated reference signals generated by the radio receiver and the motor control signals sent to the electronic speed controllers. A Padé approximation of the digital sample and hold [64] is incorporated to account for the destabilizing effect

6.4 Hardware Implementation

The quadrotor's flight control system is implemented in a Xilinx Spartan-3 field programmable gate array (FPGA) development board, pictured in Figure 6.1. The size and weight of the FPGA board are suitable for use on the moderate-sized quadrotor platform. In addition, the starter board provides a serial port for interfacing with the inertial sensor and also sufficient switches and displays to facilitate setting configuration options and diagnostics such as system status reporting. The attitude algorithm is hosted on a one million gate FPGA with a system clock operating at 50 MHz. To accommodate additional planned functionality, the footprint of the attitude algorithm was minimized where possible.
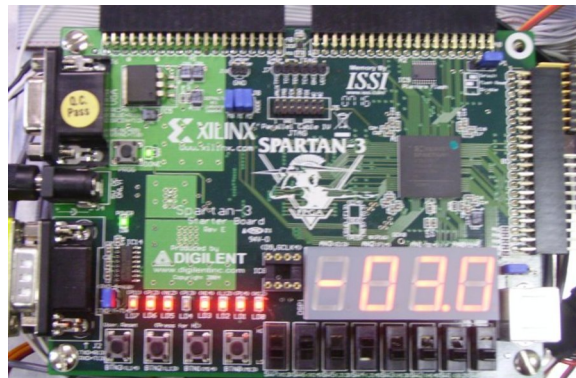

Figure 6.1: Spartan 3 FPGA Development Board

A block diagram of the system is shown in Figure 6.2. The five core functions hosted on the FPGA are the inertial and radio interfaces, the bias correction, an attitude

update algorithm, and the control loops used for stabilization. The FPGA is programmed using VHDL (VHSIC[1] Hardware Description Language). Limitations of that language are described in Section 6.4.1 and each of these five function are described in Sections 6.4.2–6.4.6.
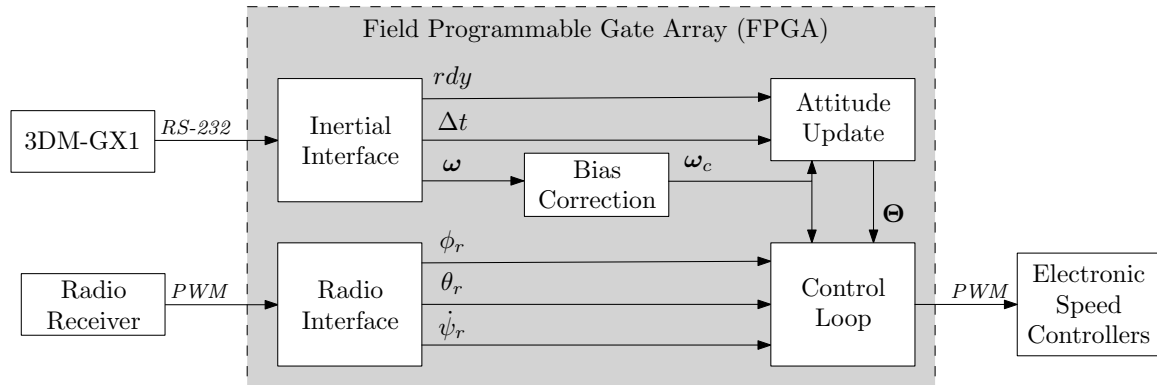
Figure 6.2: FPGA Block Diagram

6.4.1   Hardware Description Language

At first glance VHDL appears to be very similar to a typical programming language with conditional statements and loop structures. Many of these facilities, however, are of limited use; they can are provided for simulation but cannot actually be synthesized for hardware. One example is the inclusion of the *real* number type which permits VHDL floating point operations. This type cannot be synthesized, meaning that it can be simulated but not actually programmed into the FPGA.

Two work-arounds exist to permit the use of floating point operations. The first is the availability of Xilinx intellectual property (IP) cores which make available *black-box* modules that are capable of performing a single floating point operation. This option was

---

[1]VHSIC is an acronym for very high speed integrated circuit

not chosen as the IP cores generated are too large to use on the relatively small Spartan III FPGA. The second option is to use a draft version of the forthcoming Institute of Electrical and Electronics Engineers (IEEE) floating point libraries. Unfortunately those libraries cannot be used on a Xilinx FPGA since they rely on negative indices which are not supported by the Xilinx synthesis tools. Therefore, a third option was pursued which is the development of a Xilinx-compatible floating point library.

6.4.2 Inertial Interface

A generic signal interface for the inertial sensor was established to facilitate the use of other sensors in the future. This interface consists of five signals as listed in Table 6.1.

Table 6.1: Inertial Interface

Signal	Units	Type
Roll Rate	rad/s	fixed point
Pitch Rate	rad/s	fixed point
Yaw Rate	rad/s	fixed point
Delta Time	s	fixed point
RDY	N/A	boolean

At each assertion of the RDY flag, the data is processed to remove the bias and then made available for attitude determination and use in the FCS feedback loops. The angular rate and time signals are defined as fixed-point numbers with the number of bits declared in a configuration file. In this manner, the width of the interface can vary based on the resolution of the inertial unit and, by configuring the hardware description with adjustable

length ports, the FPGA synthesis tool automatically adjusts the bias correction and attitude update sections of the FPGA accordingly.

Specifically for the Microstrain 3DM-GX1, the inertial interface establishes serial port communications and places the sensor into a continuous data transfer mode. The interface also performs basic error checking and, because the Microstrain provides angular rates and time increments in 16-bit raw counts, it converts the signal to the units specified for the generic interface. The scale factor for angular rate, 17×2^{-16} is readily implemented in fixed point arithmetic using a simple multiplication followed by a shift operation. The time scale factor, $0.003 = \frac{3}{125} \times 2^{-3}$, however, cannot be implemented without introducing a rounding error. As shown in Table 6.2 a scale factor word length of ten bits or greater minimizes the degradation in accuracy.

Table 6.2: Rounding Error in the Time Scale Factor

Length	Value	Error
(bits)	(ms)	(%)
8, 9	3.91	30.21
10–12	2.93	2.34
13	3.05	1.73
14, 15	2.99	0.31
16	3.01	0.20

6.4.3 Bias Correction

The nominal 50-second initialization period, τ_i, used to determine the sensor bias is adjusted so that the mean can be implemented in hardware by a summation followed by a

simple shift operation. Because the Allan variance analysis exhibited a flat bias instability region for the interval of interest, a slight increase in the initialization period is of no consequence. If f is the sensor data rate, then the actual length of the initialization period is given by:

$$\tau'_i = \frac{2^{b_i}}{f} \tag{6.1}$$

where $b_i = \text{ceil}(\log_2(\tau_i f))$ where the ceil() operator rounds up to the next integer. The number of discrete samples included in the summation is 2^{b_i} and the decimal is shifted over b_i bits to calculate the mean. For precision, the bias and the corrected angular rates retain all fractional bits.

6.4.4 Radio Interface

Even after removing the initial bias, the bias instability and the angle random walk in the sensor will introduce a residual nonstationary error that must be manually compensated for by the pilot. With stick inputs that only cover a fixed range, the scale factor for the reference command inputs must be applied in the FPGA that is large enough to accommodate predicted error growth without unduly raising the system gain. In practice, without additional aiding the error grows without bounds and the flight ends when a full stick input is required to maintain a level attitude.

Neglecting the coupling inherent in the Euler angles, the attitude angles can be represented in a simple form as:

$$\boldsymbol{\Theta} = \int \omega t dt \tag{6.2}$$

As shown in the Allan variance analysis, the angular rate is corrupted by errors due to bias instability and angle random walk such that $\omega = \omega_t + \omega_{arw} + \omega_{bi}$, where ω_t is the true angular rate, ω_{arw} is the error in the angular rate due to angle random walk, and ω_{bi} is the error due to bias instability. In addition, the time interval contains an error due to rounding

such that $t = t_t(1 + S_r)$, where t_t is the true time and S_r is the scaling error due to rounding. Incorporating these errors into the expression for attitude yields:

$$\Theta = \int (\omega_t + \omega_{arw} + \omega_{bi}) d(t_t(1 + S_r))$$

$$= \int (\omega_t(1 + S_r) + (\omega_{arw} + \omega_{bi})(1 + S_r)) dt_t$$

$$= \Theta_t(1 + S_r) + \int (\omega_{arw} + \omega_{bi})(1 + S_r) dt_t \qquad (6.3)$$

where the first term represents a scaled version of the true attitude and the second term is the error due to both sensor noise and rounding error. Since the quadrotor flight profile that consists of only nominal excursions from a hover, the true attitude will generally remain close to zero for pitch and roll and the affect of rounding is minimal. The second term is the residual error for which the pilot must compensate. The uncertainty of this term as a function of time is:

$$\sigma_\Theta(t) = (A \sqrt{t} + Bt)(1 + S_r) \qquad (6.4)$$

Using the error coefficients from Table 3.2 and a 10-bit time scale factor, a suitable command reference scale factor can be selected that encompasses the two-sigma attitude uncertainties for roll and pitch angles. For example, from Figure 6.3 a scale factor corresponding to ± 13 degrees accommodates five minutes of flight. This duration is sufficient for many of the profiles planned for the AEC quadrotor and longer flights are accommodated by increasing the scale factor at the expense of increasing the sensitivity to the control stick.

6.4.5 Attitude Update

Based on its resolution, the sensor is capable of reporting an incremental angular change as small as 0.78 microradians. To adequately cover the dynamic range from the incremental change to a full rotation, a nonstandard floating point representation was
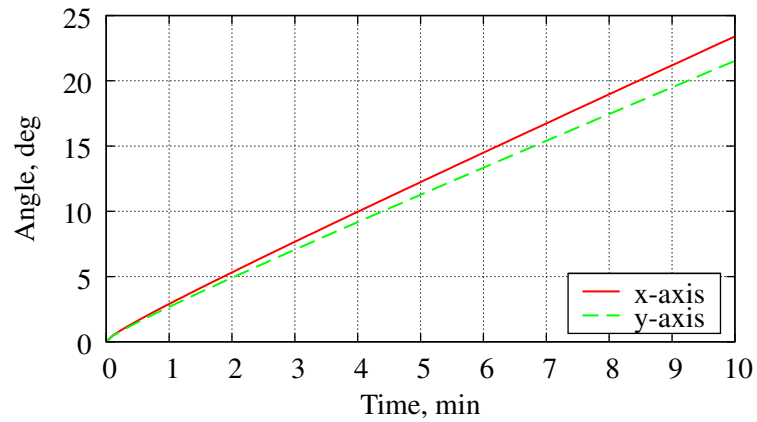
Figure 6.3: Uncertainty (2σ) in Roll and Pitch

implemented for the attitude calculations. The exponent was set at six bits to span the dynamic range, and the length of the mantissa was determined using a simulation of the FPGA algorithm. The algorithm was propagated using a brief data set collected as the inertial sensor was subjected to a series of doublets followed by a three-axis oscillation. The length of the mantissa was then determined by evaluating the incremental change in performance. As shown in Figure 6.4, a representative plot of the roll angle error, there was negligible benefit beyond 18 bits so the mantissa was set at that length.

Direct coding of the 3x3 matrix multiplication is impractical based on the requirement for 18 additions and 27 products. The resources required for each of these operations are summarized in Table 6.3 in terms of FPGA slices and dedicated 18×18 bit multipliers. Each FPGA slice contains two four-input lookup tables and two flip-flops and the Spartan-3 chip used contains 7680 slices and 24 dedicated multipliers. For comparison, the results for a 25 bit fixed point implementation is also included.

While the products can be readily implemented, and are in fact more compact than the corresponding fixed point representation, the floating point addition is prohibitively large. Therefore, the matrix multiplication is subdivided first into a series of dot products
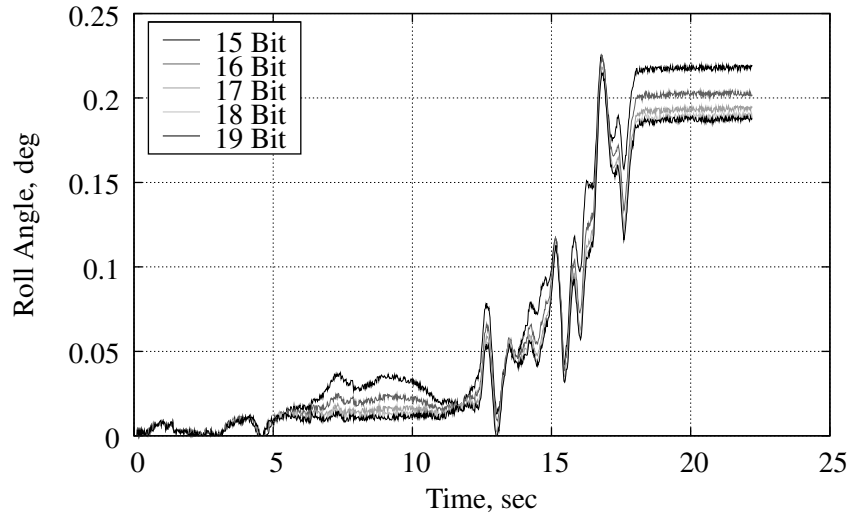
Figure 6.4: Roll Angle Error with Varying Mantissa Length

Table 6.3: FPGA Resources for Floating-Point and Fixed-Point Operations

Operation	Type	Slices	18×18 Multipliers	Latency (ns)
Addition	Float	421	0	14.3
	Fixed	27	0	7.0
Multiplication	Float	51	1	15.1
	Fixed	53	4	15.6

and then into a series of additions, each of which is carried out sequentially using the same hardware. This method, described by pseudo-code in Figure 6.5, eliminates 17 additions but at the cost of a number of multiplexers to route the signals. However, in the case of floating-point multiplication, it is advantageous to use three dedicated multipliers for the dot product rather than introduce the multiplexers. As implemented the matrix

multiplication occupies 1191 slices and 3 multipliers, corresponding to 15% and 12% of available resources, respectively.

```
C = matrix_multiplication(A,B)          C = dot_product(A,B)
  for r = 1 to 3                          product(1) = A(1)*B(1)
    for c = 1 to 3                        product(2) = A(2)*B(2)
      C(r,c) = dot_product(row(A,r),      product(3) = A(3)*B(3)
                           col(B,c))      sum = 0
    end                                   for i = 1 to 3
  end                                       sum = sum + product(i)
                                          end
```

Figure 6.5: Pseudo-Code for 3×3 Matrix Multiplication

The pitch and roll angles required for platform stabilization are extracted from the discrete direction cosine matrix, Equation (5.26), using small angle approximations and Equation (5.28). Note that the small angle approximations impact only the pitch and roll angles calculated for a specific moment in time and have no influence on the accuracy of the attitude solution carried in the direction cosine matrix, even in the case of large excursions in pitch or roll. For the quadrotor platform, pitch and roll angles are controlled to be less than eight degrees for all modes of flight and the heading is maintained solely by the pilot. Therefore, the small errors introduced by the approximations are inconsequential. For other applications it may be beneficial to implement the trigonometric functions using lookup tables or the coordinate rotation digital computer (CORDIC) algorithm [56].

6.4.6 Control Loop

The flight control system uses feedback loops, shown in Figure 6.6, to stabilize the vehicle based on the measured angular rates and the derived attitude angles. Note that with

symmetry the feedback loops for the roll channel are identical to that for the pitch channel. Feedback gains and the lead compensator were initially selected to achieve a satisfactory step response. As shown in Figure 6.7 for the baseline take off weight of 16.5 pounds, a well-damped gain settings were selected that would provide an intuitive response for novice pilots.
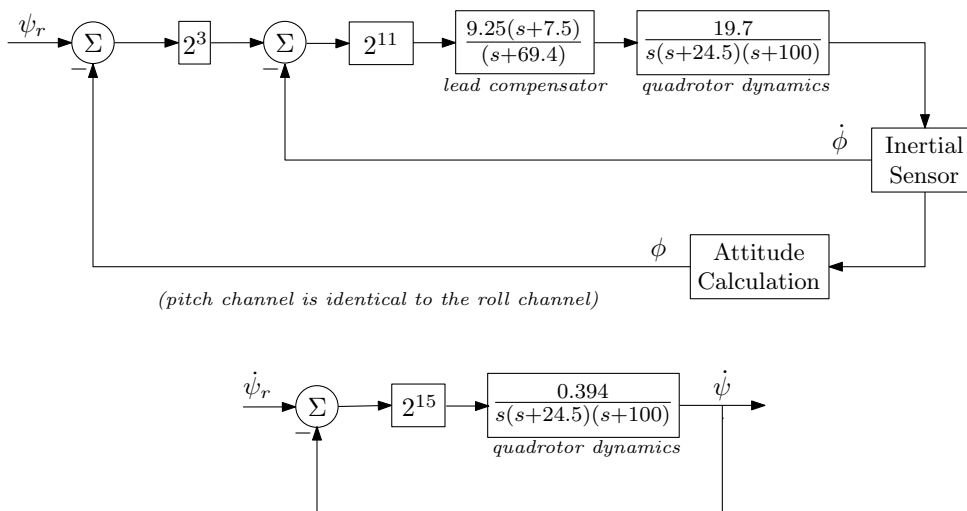

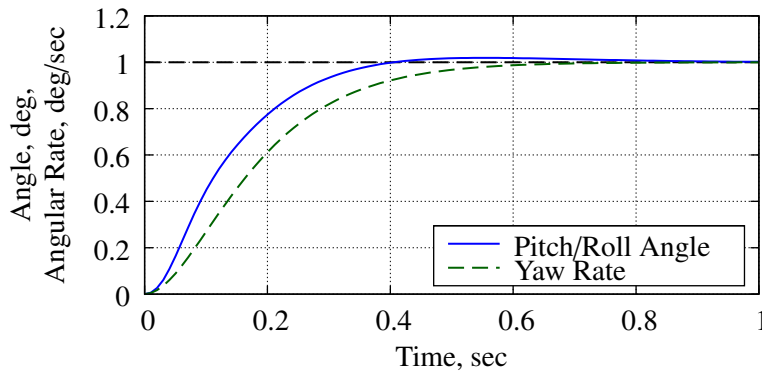Figure 6.6: Flight Control System Feedback Loops

Figure 6.7: Closed loop step response

If required, these gains can be adjusted based on take off weight and mass distribution of the planned configuration. For the payloads flown, however, the quadrotor dynamics were not found to vary significantly and a single set of gains was employed. Since the payloads are fixed during the course of a flight, there are no provisions for adjusting the gains in flight. Instead, the FPGA stores multiple sets of gains which can selected during preflight if necessary. This configuration allows flights with multiple preplanned payloads without having to reprogram the FPGA.

To facilitate implementation on the FPGA the feedback gains chosen were of the form $K = M \times 2^E$. This enabled the use of a fixed point notation using only multipliers and shift operation in the FPGA. Likewise, the lead compensator was selected so that the discrete time transfer function consisted of numerical values of the same form:

$$\mathrm{H}(z) = \frac{751 \times 2^{-7}(z - 55 \times 2^{-6})}{z - 23 \times 2^{-7}} \tag{6.5}$$

Because the quadrotor dynamics include the motor and propeller as well as the aerodynamics, the input to that block is a pulse width modulated (PWM) motor command signal that is delivered to an electronic speed controller. The standard PWM signals used for the quadrotor have a variable width component of 0-1 ms. With the FPGA operating at 50 MHz, the PWM interface is able to provide a command signal resolution of 1/50,000. The ability of the speed controller to respond to 20 ns changes was not ascertained and likely this response varies between different controllers. Nonetheless, an upper bound on the useful resolution of the attitude is determined by the closed loop gain which varies as a function of the PWM resolution. For example, the closed loop gain for the roll and pitch channels shown in Figure 6.6 is 2^{14}. In this case, angular precision, in radians, for pitch and roll beyond 14 bits will have no impact on the motor commands. Therefore pitch and

roll angles have an effective resolution of 3.5×10^{-3} degrees even though the sensor itself supports a resolution of 4.5×10^{-5} degrees.

7   TEST PREPARATION

7.1   FPGA VERIFICATION

The FPGA code was verified using a series of four simulations: an idealized *truth* model; a simulation of the FPGA logic neglecting hardware issues such as timing; a full simulation of the FPGA using Modelsim XE, a program that simulates the actual VHDL code; and execution on the actual FPGA using a simulated inertial unit to supply a deterministic profile.

7.1.1   Idealized Model

The first test evaluates the effects of first order assumptions by comparing the results of an idealized model to the lower order model implemented on the FPGA. For example, the propagation of the attitude DCM in the ideal model uses the full matrix exponential while the FPGA code uses only a first order approximation. The ideal model also utilizes higher-precision floating point numbers.

7.1.2   Logic Model

The lower order model is based on an Octave/Matlab math library[1] that is a reimplementation of the fixed point and floating point VHDL libraries used on the FPGA. This library duplicates with high fidelity the precision and rounding caused by bit limitations in the hardware. As a result, this simulation was used to rapidly evaluate the effects of bit lengths on the various signals contained in the FPGA. It also served to validate the procedures used, especially when developing and debugging the various interfaces and the attitude algorithms.

---

[1]Octave and Matlab are high-level interpretive math programs whose scripting languages are largely compatible with each other.

The development of the Octave library also allowed for rapid prototyping and debugging since the simulation of a nominal profile could be completed in only a couple minutes. The time necessary to simulate profiles using a VHDL simulator, on the other hand, sometimes took hours to complete. In both cases, the simulations were accomplished using data collected from the Microstrain 3DM-GX1 during a simulated profile.

7.1.3 Modelsim

In the third simulation, virtual test benches were executed using Modelsim and the same profile data as the logic and idealized models. Modelsim processes the VHDL code directly though it does not take into account issues such as timing delays that cannot be determined without synthesis. Parameters of interest were saved to file during the Modelsim runs and could be compared directly to either of the first two models. This simulation verified the actual implementation of the procedures in VHDL.

7.1.4 FPGA Simulation

For the last simulation, a virtual 3DM-GX1 was coded in VHDL that provided the same interface expected by the FPGA universal asynchronous receiver/transmitter (UART) component. In that manner, the presence of a simulation should have been transparent to the rest of the VHDL code. However, the simulated Microstrain was able to provide a stored subset of the same data set used for the other simulations. Comparing endpoints as reported through the development board's liquid crystal display (LCD) and light emitting diodes (LEDs) provided a measure of confidence that hardware-specific issues, such as timing, were satisfactory. An option also existed to force the FPGA into a mode where it

would single-step through a data cycle[2] which allowed for a comparison of much of the internal states to the other simulations.

7.1.5 Verification Process

The verification process involves the following steps:

1. Collect a data set while moving the 3DM-GX1 sensor through the desired profile.

2. Run Modelsim using the data set to generate the FPGA's deterministic response to the noise-corrupted data.

3. Store a limited subset of the data in a lookup table on board the FPGA and use the simulated 3DM-GX1 to feed these values to the FPGA.

4. Evaluate the FPGA results by comparing the final value and also stepped values to the Modelsim results.

5. Simulate the ideal case using the collected data set.

6. Simulate the logic model using the collected data set.

7. Compare the results of the ideal model, the logic model, and Modelsim.

7.2 BUILD UP APPROACH

In addition to simulation, the adequacy of the derived model and the suitability of the flight control system has been empirically confirmed using the *build up* (or incremental) approach. In the first step of this approach, a motor was mounted at the free end of a hinged lever arm. With the propeller inverted and the motor reversed, this configuration

---

[2]The virtual 3DM-GX1 was programmed to provide a data message only when prompted by the FPGA regardless of the delay.

served as the test stand for collecting thrust data (see Figure 7.1). With the motor mounted normally, this fixture allowed the verification of the thrust model by comparing the throttle required to the throttle predicted to maintain a level attitude. Although the dynamics of the lever arm varied significantly from the quadrotor dynamics, this initial step also served to demonstrate proper implementation of the stabilization algorithm by tracking commanded angles.
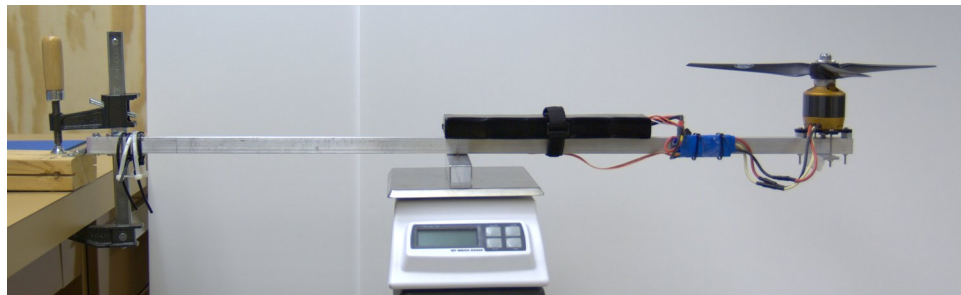

Figure 7.1: Single motor test fixture

The second step, pictured in Figure 7.2, attached a rotating shaft to one arm of the quadrotor to allow verification of performance about a single axis. The attachment point used shims that allowed the axis of rotation to be aligned with the calculated center of gravity, thus preserving the quadrotor dynamics so that performance was representative of that anticipated in flight. The center of gravity was estimated using a point mass model that accounted for the weight and location of each significant component. The proper alignment of the test fixture was confirmed by the lack of restoring moments about the shaft regardless of attitude. With the quadrotor symmetrical about the pitch and roll axis and the yaw rate generally set to zero, this fixture facilitated the fine tuning of the closed loop gains to meet desired handling qualities. Only after adequate performance was observed on the two-motor test stand was a free flight attempted.
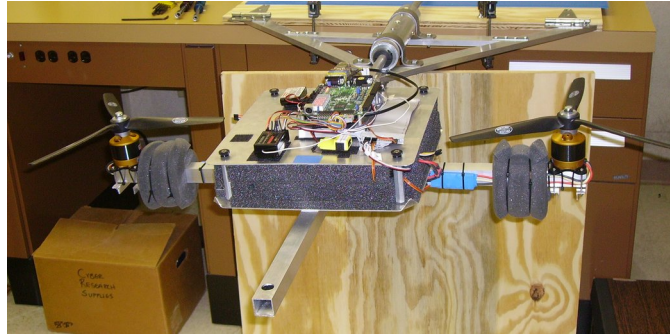
Figure 7.2: Rotating shaft test fixture

7.3 TEST HAZARD ANALYSIS

The single greatest hazard associated with the AEC quadrotor is the potential contact of the rotors. This section details specific hazards identified, the associated risks, and the steps taken to mitigate the risk. Safe flights are contingent on the adherence to the mitigation procedures identified in this section.

7.3.1 Hazard: Propeller Operating Limit

Risk: Mechanical failure / injury to persons or property

Description: The manufacturer, Master Airscrew, provides a formula for calculating the operating limit of their propellers to avoid mechanical failure

$$N_{max} = \frac{160,000}{D} \tag{7.1}$$

where D is the diameter of the propeller in inches.

Mitigation: The operating limit for the 14x7 propellers is calculated to be 11,400 RPM. Figure 7.3 plots the motor speed as a function of applied voltage both with and without the propeller. Although not directly applicable to a propeller speed limit, the motor achieves its maximum possible speed with no load attached, so it establishes the worst case condition. The maximum applied voltage of 21 VDC corresponds to the full-charge voltage

of the five cell battery packs with no load applied. Under load there is a significant drop in the voltage at the battery terminals, so the maximum motor voltage is considerably lower. As shown, the the motor speed remains safely below the operating limit at all times
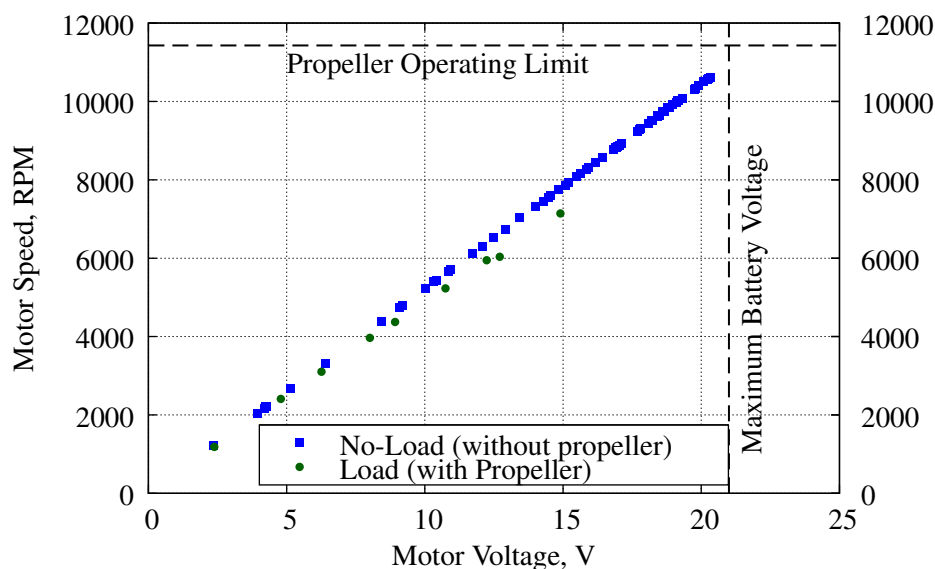
Figure 7.3: No-load motor speed

7.3.2 Hazard: Uncommanded motion at power-up

    Risk: Contact hazard / injury to persons or property

    Description: The motors spin in response to the three-phase voltage applied by the corresponding ESC and each ESC in turn receives power from a dedicated battery pack. The ESC provides a three-phase voltage level in response to a motor command signal which originates from the FCS. Although the ESC does respond with an audible cue when both power is connected and a command signal is first received, it does not offer any protection against a motor rapidly turning on if the command signal is not set to zero.

    Mitigation: The FPGA has been programmed with multiple interlocks to preclude accidental activation of the motors at power-up. Initially the FPGA sets all motor

commands to zero after each hard (power-up) or soft reset. Then, the FPGA latches the motor commands at zero until three criteria are satisfied. First, a valid radio signal is being received as indicated by the presence of all five channels. Second, the FCS has been armed by moving the Master Arm switch to the upper position. Finally, the four control channels, roll, pitch, yaw, and throttle, must be set to near zero; the threshold for the PWM being set at 20.5 μs which is below the level, approximately 100 μs, at which the motors overcome friction and begin to turn.

7.3.3 Hazard: Uncommanded motion after power-up

   Risk: Contact hazard / injury to persons or property

   Description: With the control sticks centered (roll, pitch, and yaw) or down (throttle), the flight control system will generally not have enough authority to spin up the motors. With the quadrotor idle, complacency might lead the operator to believe that the vehicle is safe and can be approached. However, if the feedback loops are still engaged as the inertial sensor drifts the FCS may become active in a misguided attempt to restore the platform to a *level* attitude.

   Mitigation: On touch down, the operator should immediately disarm the FCS by lowering the Master Arm switch. After approaching the platform, power to the FPGA board should be disconnected, effectively disabling the ESCs and the motors.

7.3.4 Hazard: Interference

   Risk: Unintended motion / injury to persons or property

   Description: Considerable interference has been noted in the lab with the Futaba radio and receiver. This was likely due to metal cabinets in close proximity and the issue was exacerbated by the antenna placement which is mounted directly to an aluminum plate.

With a lead compensator in the feedback loop, anomalous reading due to interference can lead to rapid changes in the motor commands.

Mitigation: A satisfactory range check was performed on the vehicle. With the quadrotor placed near second base at the Athens Southside Park's baseball field, the operator walked to the outfield fence with the radio antenna both extended and collapsed. With the antenna fully extended no audible hesitation in the motors was noted. With the antenna collapsed, periodic disruptions to the motors was noted.

The receiver interface was designed to be cautious in that all but the most insignificant dropouts in the PWM signal cause the corresponding channel to be set zero. Without any lift-producing surfaces, the loss of even a single channel for more than a brief moment would likely cause an immediate departure. To minimize damage to other than the quadrotor itself, the flight path should be planned to avoid flying over people or valuable property.

The PWM signal is filtered such that a signal that drops low, potentially signalling the end of the pulse, must remain low for 64 consecutive clock cycles (1.3 μs, or 0.1% maximum pulse width) before the end of the pulse width is declared. This results in a negligible delay and bias in the reported value.

A spread spectrum radio that uses multiple receiver antennas that, by design, are lifted off of the aluminum mounting plate was initially considered. Theoretically this radio should be less prone to interference. However, periodic dropouts in the received signal were detectable both on an oscilloscope and with a status LED on the FPGA board itself. As the signal filtering described earlier, it is not known at this time whether or not that process would mitigate the dropouts.

7.3.5 **Hazard**: Crossed sensor or motor signals

Risk: Uncontrollable response

Description: Although the motor leads are labeled numerically, the connectors are not keyed to prevent inadvertently swapping to leads when making the connection to the FPGA board. In addition, while an outline of the Microstrain 3DM-GX1 is drawn on the mounting plate for reference, it is possible for the sensor to be rotated when mounted. Incorrect connections of either the motors or the sensor could cause a rapid unintended response.

Mitigation: A undesired response is generally best countered by reducing the throttle as the quadrotor will fall immediately since it has no lifting surfaces. The proper installation should be confirmed prior to each flight by using the following two steps. First, with the motor batteries disconnected, lift each motor in succession and verify the correct sense in the angle or angular rates as displayed on the FPGA. Second, with the motor batteries connected, raise the throttle until the motor just turns on. Then verify that the motors respond with the correct sense to commanding roll, pitch, and yaw. For example, with a pitch up command the number one motor on the positive x-axis should increase its speed and the opposite motor should slow down or stop.

7.3.6 Hazard: Loss of power

Risk: Undesired response

Description: If the FCS were to deplete the avionics battery before the motor batteries, or if the motor batteries experienced an uneven discharge such that one depleted before the others, then the quadrotor could exhibit an undesired response.

Mitigation: Motor batteries should be used in a consistent group of four to ensure that all four batteries age at approximately the same rate. Rotating positions for the batteries, so that no single battery always powers the same motor, will help to ensure similar

aging. In practice, even when flown with no payload, the motor batteries have depleted at the same or even a faster rate than the avionics battery; however, this should be monitored over the life of the batteries as they discharge rates may vary with age.

7.3.7 Hazard: Excessive battery temperature

  Risk: Fire

  Description: When operated under a heavy load, the potential exists for the batteries to exceed their safe working temperature. The problem is exacerbated by the AEC quadrotor design which removes the batteries from the free air and surrounds them with foam.

  Mitigation: Using a fixture in the lab, one of the motor batteries was allowed to discharge with a current draw of approximately 42 amps. A temperature probe was attached to the battery which was not in an enclosure. The battery temperature, as shown in Figure 7.4, reached the upper bound of the operating range but remained below the maximum discharge temperature limit. As a precaution, the foam that surrounds the batteries has been modified to permit better air circulation. Also, an EagleTree data logger is now used regularly to record the temperature for post-mission analysis. Long duration, high payload mission are not advised until the temperature rise on a battery within the enclosure is better analyzed.

7.4 MISSION PLANNING

The power losses detailed in this dissertation are summarized in Fig. 7.5 as a percentage of the total power consumed from the battery. Under a light load, the loss is dominated by the rotational losses but at greater leads, corresponding to high motor speeds, the internal
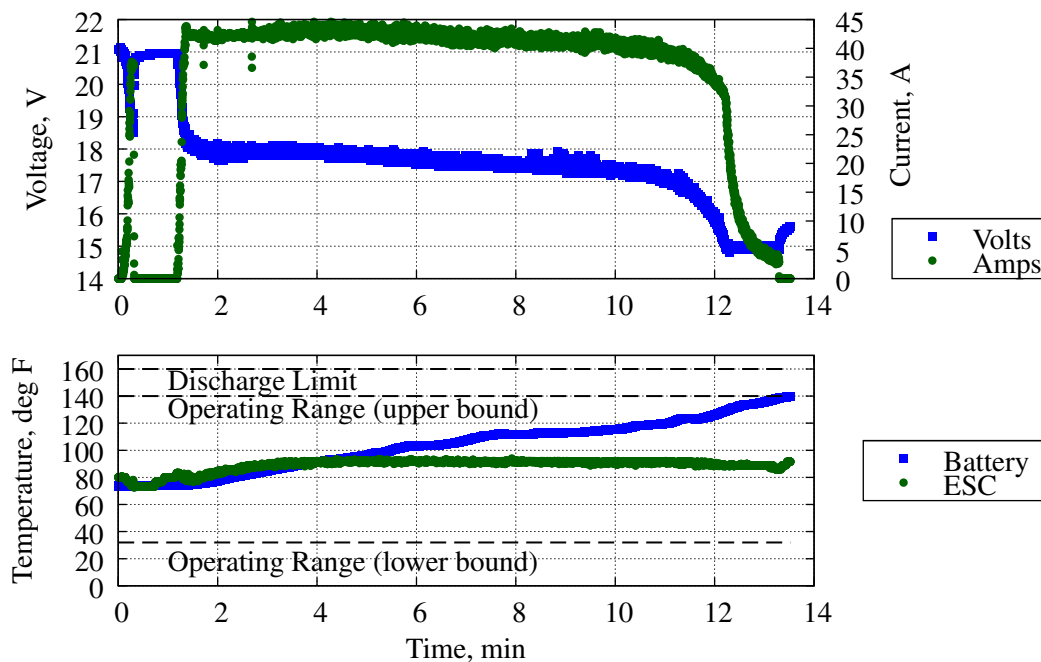
Figure 7.4: Battery characteristics for a 42 A load

resistance of the battery plays an increasing factor accounting for half of the losses. As expected, the losses associated with the electronic speed controller are negligible.

The power loss associated with the internal resistance of the battery pack imposes two limitations on flight time. First, with over 100 W of power dissipated as heat under a 40 A load, the maximum operating temperature may be exceeded unless sufficient cooling is provided. In the lab, a 42 A load resulted in a battery pack approaching the 140° F limit after ten minutes of continuous operation. As a result, the battery enclosure was modified to better facilitate passive cooling and additional testing using the battery enclosure is recommended for further study.

The second limitation is the decrease in available battery capacity due to the internal power loss which can account for over 13% of the power consumed. A chart, such as Fig. 7.6, is a convenient tool that can be used to determine the resulting flight duration
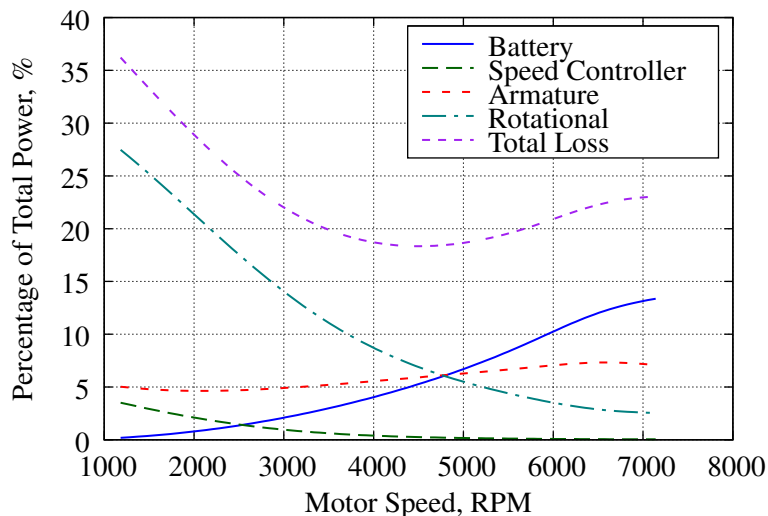
Figure 7.5: Component losses as a percentage of total power

as a function of required thrust. In use, the left chart gives the total power required to hover as a function of vehicle weight. The right chart then provides the battery current for each motor and the flight duration that corresponds to that power level. Additionally, the power dissipated as heat in the four battery packs is graphically illustrated as the difference between the power consumed and the power required curves. As an example, the quadrotor with a ten pound payload requires nearly 3 kW of power. This power level corresponds to 505 W dissipated as heat, a 42.5 A current draw, and over 9 minutes of flight. Note that the power required curve in Fig. 7.6 includes an adjustment to account for the loss in propeller efficiency when installed on the quadrotor compared to the efficiency measured on the thrust test stand. An 11% reduction in efficiency was calculated from flight test data collected with payloads ranging from 0 to 10.5 pounds.
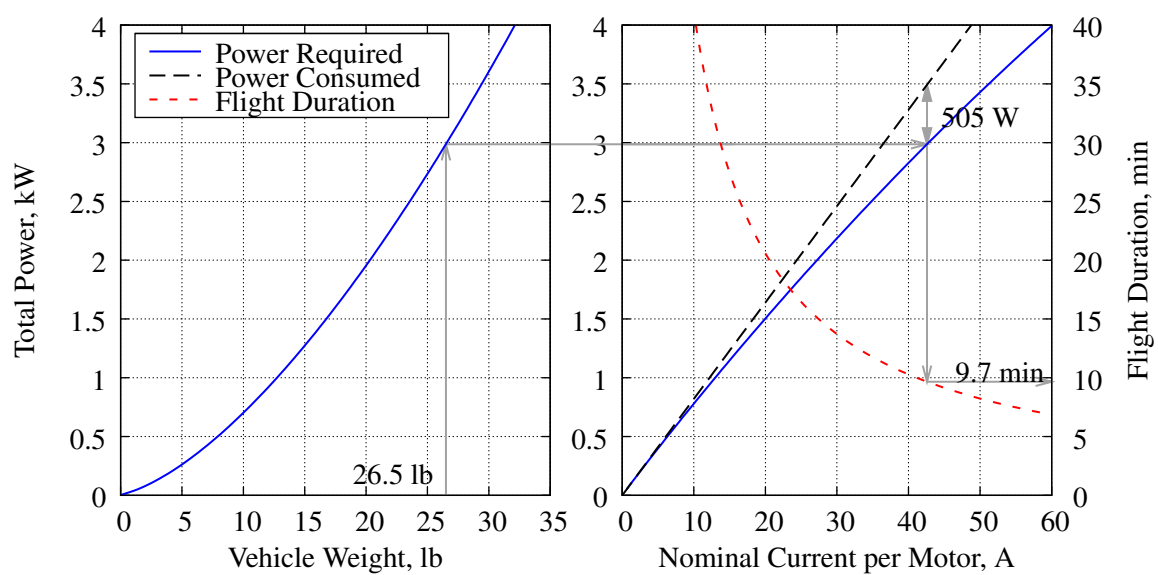
Figure 7.6: Flight duration as a function of vehicle weight

8 RESULTS

8.1 ATTITUDE DETERMINATION

A Monte Carlo analysis confirmed that measured data matched the error model described by Equation (6.4), validating the use of the Allan variance to estimate noise coefficients. Figure 8.1 shows the roll angle Monte Carlo plot and the predicted and calculated statistics. The pitch axis exhibits similar characteristics with yaw axis having somewhat worse performance as anticipated by the noise coefficients in Table 3.2. The data were collected from a stationary sensor and the Euler angles were calculated using the FPGA algorithm after compensating for the bias from the angular rates as previously described. As expected, there is significant error growth due to the bias instability even for short time periods.
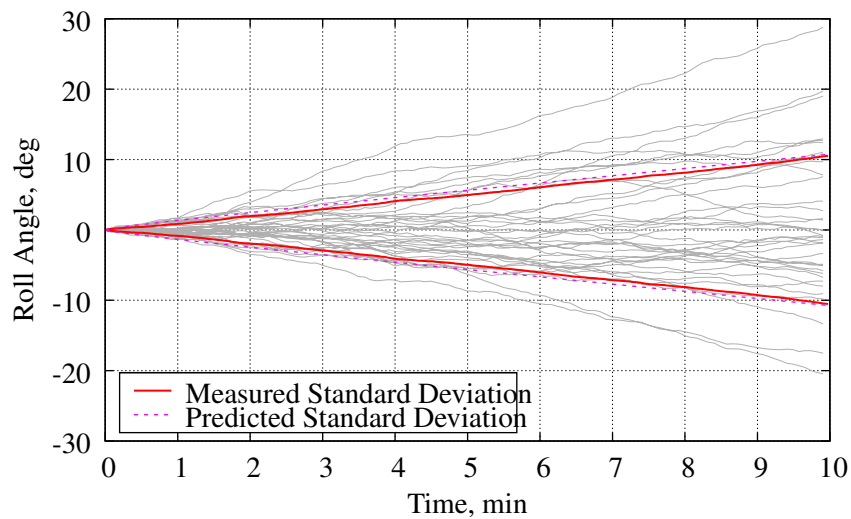

Figure 8.1: Monte Carlo analysis (37 runs)

Figure 8.2 plots the standard deviation of the Monte Carlo analysis for each channel and the device accuracy specification for dynamic maneuvering. The dynamic accuracy

was not measured due to current limitations in the data collection setup for the quadrotor. However, a Monte Carlo analysis for the static condition was completed and the one-sigma parameters were found to be in general agreement with the specifications: 0.60°, 0.56°, and 0.98° for roll, pitch, and yaw, respectively, compared to a specification of 0.5°. Furthermore, because the attitude algorithm is not based on the accelerometers, unlike the solution embedded in the sensor, the results are expected to be representative of dynamic performance.

Two conclusions can be drawn from Figure 8.2. First, for the first two minutes the gyro-based solution implemented on the FPGA outperforms the dynamic-maneuvering specification. Second, the growth is slow enough that the drift can easily be corrected by the pilot. The operational limit for mission duration is then based on the scale factor applied to the command reference input. As long as the pilot can compensate for the drift using trim or manual inputs, the performance remains satisfactory.
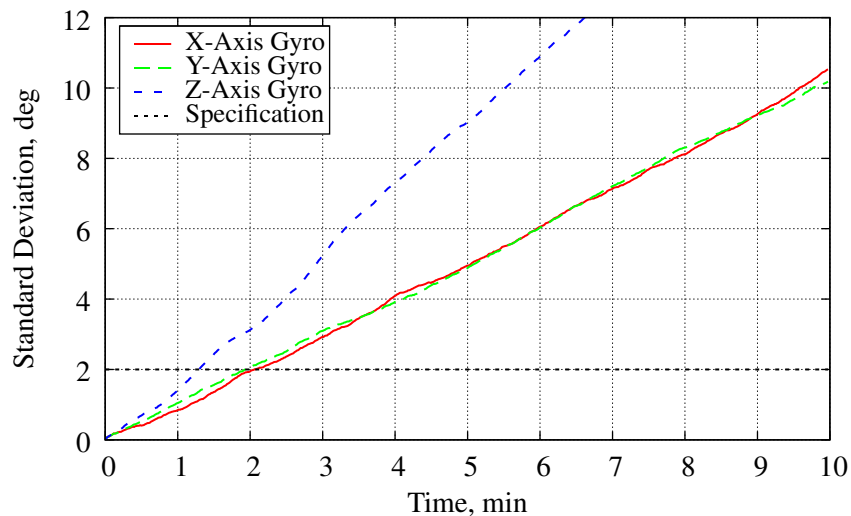

Figure 8.2: Statistical Comparison of Attitude Methods

8.2 FIRST FLIGHT

The first attempt was unsuccessful with the quadrotor showing a tendency to raise on one arm and eventually flip with increasing throttle. This led to a thorough review of the stabilization algorithm and it's implementation on the FPGA. In addition, the variation between motors was considered since this design does not use closed loop control to assure matched motor speeds. With no anomalies noted, ground effect was assumed to be the cause. Therefore, a launch platform was built using a wire mesh that allowed the quadrotor to be launched away from the ground without significant disturbance to the airflow. This solution proved satisfactory as the quadrotor launched from the platform and flew exceptionally well on the second attempt, Fig. 8.3.

Figure 8.3: Initial flight configuration without payload or carbon fiber frame

The ground effect for a helicopter is considered a significant factor up to a height of one rotor blade [4], and it has been demonstrated that once airborne the quadrotor can be flown across the ground at heights close to one blade length. Ground effect was not an issue on landing where the power was reduced and the quadrotor quickly transited through the ground effect. Subsequent flights were flown with a carbon fiber frame which attaches

beneath the quadrotor. This frame serves as both a protective structure for the payload and as landing struts, eliminating the need for the launch platform.

8.3 FLIGHT CONTROL SYSTEM SUITABILITY

Overall flight test results were consistent with anticipated performance. With the FPGA augmenting the quadrotor's stability, the operator was able to maintain a hover or maneuver the quadrotor with little difficulty. Compensating for sensor drift using the trim switches on the radio controller was not practical, but compensating for the drift by holding a non-zero stick input was not problematic. Over time, the drift in attitude would saturate one of the controls. However, it was not necessary to preemptively land as the drift was slow enough that the vehicle could still be brought down safely.

On two occasions the quadrotor lifted off with a slight pitch or roll rate. Because even small angles induce an acceleration by tipping the lift vector into the horizontal plane, this led to an unexpected translation and the operator opted to immediately land. The cause may be attributed to a chance offshoot in the angular rates, but with the data recording currently limited this could not be conclusively verified. The post-flight data did show a large bias in the indicated channel, but this could also have been the result of the hard landing saturating the gyroscope. In addition, the motors occasionally experience a brief jitter in power on the order of a second in duration. The attitude is largely unaffected, though there is a audible increase in motor speed, and no command inputs are necessary. Possibly a spike in the sensor noise is amplified by the lead compensator only to be immediately compensated by the feedback loop. A wireless Ethernet board has been purchased that is capable of accommodating a serial data stream from the FPGA board, an Ethernet data stream from the LADAR, and an additional serial data stream from another future sensor. When integrated,

the board will enable real time monitoring as well as post-mission analysis for anomaly resolution.

8.4 PAYLOAD CAPACITY

To characterize performance under a range of payloads, a container was attached using the LADAR mounting bracket on the bottom of the quadrotor, Figure 8.4. By varying the amount of lead shot placed in the container, the payload weight could be set at an arbitrary amount up to 10.6 pounds. Specific payloads flown are 0 lb, 3.1 lb, 4.7 lb, 6.1 lb, and 10.6 lb.

Updating the component mass properties to include the additional weight yielded only a minor change in quadrotor's mass properties. Additional weight required a higher nominal thrust setting for each motor, which in turn results in a slightly higher gain contribution by the motor. The effect of this gain, however, was largely offset by a corresponding increase in moment of inertia. Overall, there was minimal impact to the open loop system gain. Therefore, a single set of gains is used for all five payloads.

Figure 8.4: Flying with a mass simulating the LADAR

Figure 8.5: LADAR installed on the quadrotor

Pilot comments indicate that the handling qualities improves with payload. At 4.7 lb and 6.1 lb, the quadrotor was reported to feel more stable and the handling was improved. For reference, the 6.1 lb payload simulates to the weight of the SICK LD-OEM1000 LADAR with batteries and a telemetry system. Flying at the Athens Southside Park, the quadrotor with the 6.1 lb payload was flown into the outfield and back with a nice smooth motion that would be well suited for LADAR research.

In addition, the quadrotor had sufficient thrust to lift the 10.6 lb payload. The platform entered into a single significant oscillation immediately after takeoff. The oscillations disappeared without intervention and the quadrotor continued to demonstrate a stable hover. The pilot performed limited maneuvering, commenting that the handling qualities were degraded but that power available was sufficient.

During a subsequent flight at maximum payload, however, the quadrotor entered into the same oscillation but then pitched over and crashed. Insufficient data is available to determine the cause. However, the automatic recalibration discussed in Section 3.2 may well have been a contributing factor. Although the quadrotor has demonstrated the ability to lift payloads up to 10.6 pounds, additional flights at that weight are not recommended until the telemetry system is in place to qualitatively evaluate performance.

9 CONCLUSIONS AND RECOMMENDATIONS

9.1 CONCLUSIONS

This flight test effort represents the successful flight of the first unmanned high-payload quadrotor, with a payload capacity three times greater than contemporary designs. Furthermore, at full payload, this sensor platform is the largest unmanned quadrotor to achieve untethered free flight.

The system exploits the desirable characteristics of a low-cost inertial sensor, including sensor calibration and a digital interface, but demonstrates that undesirable attributes, such as susceptibility to interference and a reliance on potentially destabilizing filters, can be bypassed without unduly impacting performance. Results were quantitatively evaluated using the results of an Allan variance analysis. Ultimately, the method was proven by the successful stabilization of the quadrotor in free flight based on the derived Euler angles.

Although the results of the Monte Carlo simulation show that the uncertainty in the attitude solution varies greatly over time, the variation has been shown to be manageable for profiles suitable for sensors research. The integration of a telemetry downlink will provide data to support a more detailed analysis of the inertial sensor and the quadrotor's performance. The results of this research demonstrates that this, and similar inertial sensors, can be employed in high power, airborne platforms where the noisy electromagnetic environment would otherwise render them unusable.

The use of high power brushless motors dictated the development of new models for the electronic speed controller and the brushless motors. An automatic recalibration of the electronic speed controller was noted and may become a factor when flying near full throttle. A method of modeling rotational loss as a function of motor speed was introduced, but it was found to have no significant advantages in the operating region for this quadrotor.

Power dissipation within the battery packs due to internal resistance, on the other hand, was determined to be significant and the limiting factor in flight duration. Another impact to flight time is the temperature rise noted in the batteries.

A novel method of predicting sortie duration as a function of payload weight was presented. The accuracy of this method hinged on the detailed component models developed. Real time estimates of power remaining are difficult with fluxuating loads and lithium polymer batteries, which have a characteristic steep end point drop-off. Therefore, the accurate prediction of sortie duration, as presented here, is likely the most accurate and reliable information available. Neglecting the power loss internal to the battery, as presented in this dissertation, would lead to an overly optimistic estimate that could result in loss of the platform, particularly with a rotary wing aircraft that has no lift-generating surfaces.

Based on successful flight tests, classical control theory proved sufficient to stabilize the quadrotor attitude for low dynamic flight. Even allowing for a floating-point implementation and propagating the attitude using the resource-intensive direction cosine matrix algorithm, optimized code allowed an accurate solution based on a single low-cost FPGA board with room for expansion. Implementing the flight control system without relying on GPS, as with other autopilots, directly supports ongoing research into GPS denied areas. The use of the FPGA also facilitates the reuse of existing FPGA modules already created for LADAR research, such as time-stamping of LADAR data.

9.2 FUTURE WORK AND RECOMMENDATIONS

Follow-on work with this quadrotor has already begun with the integration of a telemetry system for real time data monitoring and post-mission analysis. This will facilitate a better characterization of performance, possibly including real time monitoring

of temperatures, and support anomaly resolution. Additional areas of interest include characterizing the suitability of the quadrotor design as a gimbaling platform for sensor pointing, the design of flight profiles suitable for LADAR navigation given the limitations of the quadrotor aerodynamics, specifically the constraint that attitude and position cannot be independently controlled. An analysis of the quadrotor performance when flying in off-nominal conditions, as might be dictated by the aforementioned flight profiles, is also of interest especially as they relate to the gyroscopic effects from the motors. Certainly, the ability to flight test LADAR-related algorithms developed at the Avionics Engineering Center should be a priority.

In addition, the following specific recommendations are provided to improve safety and address recently published certification requirements:

1. Add a fiberglass or carbon-fiber shell to enclose the rotor disks. This single recommendation would greatly enhance safety both in the lab and in flight.

2. Determine the temperature characteristics for batteries located within an enclosure when operated under a range of loads. Use this information to establish the permissible sortie length for various payload configurations. Until additional temperature analysis is available, limit flight duration to less than six minutes when flying with a payload greater than five pounds. This limit is based on an observed temperature rise of eight degrees per minute under moderate load.

3. Monitor the new FAA certification requirements for unmanned aircraft (UA). Effective March 13, 2008, certification is mandatory for all UA except for "hobbyists and amateur model aircraft users when operating systems for sport and recreation." [2, 65]

With a ten pound payload capacity, this quadrotor provides the Avionics Engineering Center with a new capability for testing airborne sensors. Directly intended to support LADAR research at Ohio University, the platform is equally well suited for other sensors, such as vision based navigation and wide baseline GPS attitude determination. In addition, the Air Force Institute of Technology (AFIT) and the Air Force Research Laboratory (AFRL) have both expressed an interest in the platform for sensors-related research. As a high payload platform well suited for indoor or urban navigation, the AEC quadrotor offers a unique capability for sensors research unmatched elsewhere.

REFERENCES

[1] Office of the Secretary of Defense. "Unmanned Aircraft Systems Roadmap 2005-2030". Technical report, Department of Defense, Aug. 4, 2005.

[2] Aviation Safety Unmanned Aircraft Program Office AIR-160. "Unmanned Aircraft Systems Operations in the U.S. National Airspace System". Interim Operational Approval Guidance 08-01, Federal Aviation Administration, Mar. 13, 2008.

[3] Andrey Soloviev and Maarten Uijt de Haag. "Three-Dimensional Navigation of Autonomous Vehicles Using Scanning Laser Radars: Concept and Initial Verification". *IEEE Transactions of Aerospace and Electronic Systems*, Accepted for publication 2008.

[4] John Fay. *The Helicopter*, 3rd ed. David & Charles, North Pomfret, Vermont, 1976.

[5] Charles Gablehouse. *Helicopters and Autogiros*. J. B. Lippencott Company, Philadelphia, 1969.

[6] C. V. Glines. "The Flying Octopus". *Air Force Magazine*, vol. 73, no. 10, Oct. 1990.

[7] Piasecki Aircraft Corporation. "History - Unmanned Air Vehicles (UAVs): Model PA-4". Online: http://www.piasecki.com/pa-4.htm (accessed Sep. 1, 2008).

[8] Gabe Hoffmann, Dev Gorur Rajnarayan, Steven L. Waslander, David Dostal, Jung Soon Jang, and Claire J. Tomlin. "The Stanford Testbed of Autonomous Rotorcraft for Multi Agent Control (STARMAC)". In *Proceedings of the 23rd Digital Avionics Systems Conference*, vol. 2, Salt Lake City, Utah, Oct. 24–28, 2004.

[9] Glenn P. Tournier, Mario Valenti, Jonathan P. How, and Eric Feron. "Estimation and Control of a Quadrotor Vehicle Using Monocular Vision and Moiré Patterns". In *AIAA Guidance, Navigation, and Control Conference*, Keystone, Colorado, Aug. 21–24, 2006.

[10] L. A. Young, E. W. Aiken, V. Gulick, R. Mancinelli, and G. A. Briggs. "Rotorcraft as Mars Scouts". In *Aerospace Conference Proceedings*, Big Sky, Montana, Mar. 9–16, 2002.

[11] Brian Thompson. "Full Throttle to Mars". *Rotor&Wing,* Phillips Business Information, LLC, Potomac, Maryland, Mar. 2001.

[12] Paul Marks. "Miniature Spy Helicopter Aims to Hover Unheard". *New Scientist*, vol. 180, no. 2424, p. 27, Dec. 6, 2003.

[13] Microdrones GmbH. "MD4-200". Online: http://www.microdrones.com/md4-200.html (accessed Sep. 1, 2008).

[14] Draganfly Innovations. "Draganflyer V Ti Pro". Online: http://www.rctoys. com/rc-products-catalog/RC-HELICOPTERS-DRAGANFLYER-VTI-PRO.html (accessed Sep. 1, 2008).

[15] Microdrones GmbH. "MD4-1000". Online: http://www.microdrones.com/ md4-1000.html (accessed Sep. 1, 2008).

[16] P. Pounds, R. Mahoney, P. Hynes, and J. Roberts. "Design of a Four-Rotor Aerial Robot". In *Proceedings of the Australasian Conference on Robotics and Automation*, pp. 145–150, Aukland, Australia, Nov. 27–29, 2002.

[17] Paul Pounds, Robert Mahoney, Joel Gresham, Peter Corke, and Jonathan Roberts. "Towards Dynamically-Favourable Quad-Rotor Aerial Robots". In Nick Barnes and David Austin, editors, *Proceedings of the Australasian Conference on Robotics and Automation*, Canberra, Australia, Dec. 6–8, 2004.

[18] Paul Pounds, Robert Mahoney, and Peter Corke. "Modelling and Control of a Quad-Rotor Robot". In Bruce MacDonald, editor, *Proceedings of the Australasian Conference on Robotics and Automation*, Aukland, New Zealand, Dec. 6–8, 2006.

[19] Scott D. Hanford, Lyle N. Long, and Joseph F. Horn. "A Small Semi-Autonomous Rotary-Wing Unmanned Air Vehicle (UAV)". In *Infotech@Aerospace*, Washington D.C., Sep. 26–29, 2005. AIAA.

[20] Llan Kroo and Peter Kunz. "Development of the Mesicopter - A Miniature Autonomous Rotorcraft". In *Proceedings of the American Helicopter Society Vertical Lift Aircraft Design Conference*, San Francisco, California, Jan. 2000.

[21] N Guenard, T. Hamel, and V. Moreau. "Dynamic modeling and intuitive control strategy for an "X4-flyer"". In *International Conference on Control and Automation*, pp. 141–146, Budapest, Hungary, Jun. 26–29, 2005.

[22] Samir Bouabdallah and Roland Siegwart. "Towards Intelligent Miniature Flying Robots". In *Proceedings of Field and Service Robotics*, Port Douglas, Australia, Jul. 29–31, 2005.

[23] M. S. Kang, S. Park, H. G. Lee, D. H. Won, and T. J. Kim. "Development of a Hovering Robot System for Calamity Observation". In *Proceedings of the International Conference on Control, Automation and Systems*, pp. 580–585, Gyeong Gi, Korea, Jun. 2–5, 2004.

[24] Gabriel M. Hoffmann, Haomiao Huang, Steven L. Waslander, and Claire J. Tomlin. "Quadrotor Helicopter Flight Dynamics and Control: Theory and Experiment". In *AIAA Guidance, Navigation and Control Conference*, pp. 1–20, Hilton Head, South Carolina, Aug. 20–23, 2007.

[25] *How It Works — The PPM Radio Control System*. The Model Electronics Company, Berkshire, United Kingdom, Jan. 24, 2001.

[26] Dennis P. Bobay and Glen C. Young. "Motor with External Rotor". United States Patent 5,962,938, Oct. 5, 1999.

[27] E. Spooner and L. Haydock. "Vernier Hybrid Machines". *IEE Proceedings Electric Power Applications*, vol. 150, no. 6, pp. 655–662, Nov. 2003.

[28] Norman S. Nise. *Control Systems Engineering*. Benjamin/Cummings Publishing Company, Inc., New York, 1992.

[29] James W. Nilsson. *Electric Circuits*, 3rd ed. Addison-Wesley Publishing Co., New York, 1990.

[30] Charles A. Holt. *Introduction to Electromagnetic Fields and Waves*. John Wiley & Sons, Inc., New York, 1963.

[31] Stephen J. Chapman. *Electric Machinery Fundamentals*, 2nd ed. McGraw-Hill, Inc., New York, 1991.

[32] Robert J. Boucher. *Electric Motor Handbook*. AstroFlight, Inc., 1994.

[33] Magnetics. "Ferrite Cores Catalog". Pittsburgh, Pennsylvania, 2006.

[34] Kapil Venkatachalam, Charles R. Sullivan, Tarek Abdallah, and Hernán Tacca. "Accurate Prediction of Ferrite Core Loss with Nonsinusoidal Waveforms Using Only Steinmetz Parameters". In *Proceedings of the IEEE Workshop on Computers in Power Electronics*, pp. 36–41, Jun. 3–4, 2002.

[35] Fang Deng. "An Improved Loss Estimation for Permanent Magnet Brushless Machines". *IEEE Transactions on Energy Conversion*, vol. 14, no. 4, pp. 1391–1395, December 1999.

[36] Dan M. Ionel, Mircea Popescu, Stephen J. Dillinger, T.J.E Miller, Robert J. Heideman, and Malcolm I. McGilp. "On the Variation With Flux and Frequency of the Core Loss Coefficients in Electrical Machines". *IEEE Transactions on Industry Applications*, vol. 42, no. 3, pp. 658–667, May. 2006.

[37] Kiroaki Toda, Kunihiro Senda, and Masayoshi Ishida. "Effect of Material Properties on Motor Iron Loss in PM Brushless DC Motor". *IEEE Transactions on Magnetics*, vol. 41, no. 10, pp. 3937–3939, Oct. 2005.

[38] Peng Rong and Massoud Pedram. "An Analytical Model for Predicting the Remaining Battery Capacity of Lithium-Ion Batteries". *IEEE Transactions on Very Large Scale Integration Systems*, vol. 14, no. 5, pp. 441–451, May. 2006.

[39] J. Gordon Leishman. *Principles of Helicopter Aerodynamics*, 2nd ed. Cambridge University Press, New York, 2006.

[40] *Detailed Specifications for 3DM-GX1*. Microstrain, Inc., Williston, VT, Retrieved May 28, 2008.

[41] A. Mancini, F. Caponetti, A. Monteriù, E. Frontoni, P. Zingaretti, and S. Longhi. "Safe Flying for an UAV Helicopter". In *Proceedings of the 15th Mediteranean Conference on Control & Automation*, pp. 1–6, Athens, Greece, Jul. 27–29, 2007.

[42] Jan Wendel, Oliver Meister, Chritian Schlaile, and Gert F. Trommer. "An Integrated GPS/MEMS-IMU Navigation System for an Autonomous Helicopter". *Aerospace Science and Technology*, vol. 10, no. 6, pp. 527–533, Sep. 2006.

[43] William E. Green and Paul Y. Oh. "Autonomous Hovering of a Fixed-Wing Micro Air Vehicle". In *Proceedings of the 2006 IEEE International Conference on Robotics and Automation*, pp. 2164–2169, Orlando, Florida, May. 2006.

[44] David Vissière, Alain Martin, and Nicolas Petit. "Using Magnetic Disturbances to Improve IMU-Based Position Estimation". In *Proceedings of the European Control Conference*, pp. 2853–2858, Kos, Greece, Jul. 2–5, 2007.

[45] Daniel Cruz, James McClintock, Brent Perteet, Omar A.A. Orqueda, Uyan Cao, and Rafael Fierro. "Decentralized Cooperative Control". *IEEE Control Systems Magazine*, pp. 58–78, Jun. 2007.

[46] D. L. Churchill and S. W. Arms. *3DM-GX1 Gyro Enhanced Orientation Sensor FAQ's*. Microstrain, Inc., Williston, VT, Jun. 14, 2005.

[47] *3DM-GX1 Data Communications Protocol, Version 3.1.00*. Microstrain, Inc., Williston, VT, Jul. 5, 2005.

[48] *3DM-GX1 Orientation Sensor: Fastest Data Output Rates*. Microstrain, Inc., Williston, VT, 2006.

[49] Lawrence C. Ng and Darryll J. Pines. "Characterization of Ring Laser Gyro Performance Using the Allan Variance Method". *Journal of Guidance, Control, and Dynamics*, vol. 20, no. 1, pp. 211–214, Jan.–Feb. 1997.

[50] Naser El-Sheimy, Haiying Hou, and Xiaoji Niu. "Analysis and Modeling of Inertial Sensors Using Allan Variance". *IEEE Transactions on Instrumentation and Measurements*, vol. 57, no. 1, pp. 140–149, Jan. 2008.

[51] Robert C. Nelson. *Flight Stability and Automatic Control*. McGraw-Hill, Inc., New York, 1989.

[52] John H. Blakelock. *Automatic Control of Aircraft and Missiles*, 2nd ed. John Wiley & Sons, Inc., New York, 1991.

[53] *Flying Qualities Testing*. Air Force Flight Test Center, Edwards Air Force Base, California, Sep. 17, 2000.

[54] Irving H. Shames. *Mechanics of Fluids*, 2nd ed. McGraw-Hill Publishing Company, New York, 1982.

[55] D. H. Titterton and J. L. Weston. *Strapdown Inertial Navigation Technology*, 2nd ed., vol. 207 of *Progress in Astronautics and Aeronautics*. American Institute of Aeronautics and Astronautics, Inc., Reston, Virginia, 2004.

[56] Ray Andraka. "A Survey of CORDIC Algorithms for FPGA Based Computers". In *Proceedings of the Sixth ACM/SIGDA International Symposium on Field-Programmable Gate Arrays (FPGA '98)"*, pp. 191–200, Monterey, California, Feb. 22–24, 1998.

[57] Kenneth R. Britting. *Inertial Navigation Systems Analysis*. Wiley-Interscience, New York, 1971.

[58] M. Chen and Mihai Huzmezan. "A Simulation Model and H_∞ Loop Shaping Control of a Quad Rotor Unmanned Air Vehicle.". In *Proceedings of the IASTED International Conference on Modelling, Simulation and Optimization*, pp. 320–325, Banff, Canada, Jul. 2–4, 2003.

[59] Pedro Castillo, Alejandro Dzul, and Rogelio Lozano. "Real-Time Stabilization and Tracking of a Four-Rotor Mini Rotorcraft". In *IEEE Transactions on Control Systems Technology*, vol. 12, pp. 510–516, Jul. 2004.

[60] Young Soo Suh. "Robust Control of a Quad-Rotor Aerial Vehicle". *International Journal of Applied Electromagnetics and Mechanics*, vol. 18, no. 1-3, pp. 103–114, 2003.

[61] Edinç Altuğ and Camillo Taylor. "Vision-based Pose Estimation and Control of a Model Helicopter". In *Proceedings of the IEEE International Conference on Mechatronics*, pp. 316–321, Istanbul, Turkey, Jun. 3–5, 2004.

[62] S. Bouabdallah, A. Noth, and R. Siegwart. "PID vs LQ Control Techniques Applied to an Indoor Micro Quadrotor". In *Proceedings of the IEEE International Conference on Intelligent Robots and Systems*, vol. 3, pp. 2451–2456, Sendai, Japan, Sep. 28, 2004.

[63] Henrik B. Christophersen, R.Wayne. Pickell, James C. Neidhoefer, Adrian A. Koller, K. Kannan Suresh, and Eric N. Johnson. "A Compact Guidance, Navigation, and

Control System for Unmanned Aerial Vehicles". *Journal of Aerospace Computing, Information, and Communication*, vol. 3, pp. 187–213, May 2006.

[64] John J. D'Azzo and Contantine H. Houpis. *Linear Control System Analysis and Design*, 3rd ed. McGraw-Hill, Inc., New York, 1988.

[65] Nicholas Sabatini. "Unmanned Aircraft Systems Operations in the U.S. National Airspace System". Federal Register Notice FAA-2006-25714, Federal Aviation Administration, Feb. 6, 2007.